




5-2012

Atomistic Simulations of the Fusion-Plasma Material Interface

Mostafa Jon Dadras
jonny@chem.ucla.edu

Follow this and additional works at: https://trace.tennessee.edu/utk_graddiss

 Part of the [Atomic, Molecular and Optical Physics Commons](#), [Materials Chemistry Commons](#), and the [Other Physics Commons](#)

Recommended Citation

Dadras, Mostafa Jon, "Atomistic Simulations of the Fusion-Plasma Material Interface. " PhD diss., University of Tennessee, 2012.
https://trace.tennessee.edu/utk_graddiss/1287

This Dissertation is brought to you for free and open access by the Graduate School at TRACE: Tennessee Research and Creative Exchange. It has been accepted for inclusion in Doctoral Dissertations by an authorized administrator of TRACE: Tennessee Research and Creative Exchange. For more information, please contact trace@utk.edu.

To the Graduate Council:

I am submitting herewith a dissertation written by Mostafa Jon Dadras entitled "Atomistic Simulations of the Fusion-Plasma Material Interface." I have examined the final electronic copy of this dissertation for form and content and recommend that it be accepted in partial fulfillment of the requirements for the degree of Doctor of Philosophy, with a major in Physics.

Joseph H. Macek, Major Professor

We have read this dissertation and recommend its acceptance:

Predrag S. Krstic, Adolfo G. Eguiluz, Robert J. Harrison

Accepted for the Council:

Carolyn R. Hodges

Vice Provost and Dean of the Graduate School

(Original signatures are on file with official student records.)

To the Graduate Council:

I am submitting herewith a dissertation written by Mostafa Jon Dadras entitled “Atomistic Simulations of the Fusion-Plasma Material Interface.” I have examined the final electronic copy of this dissertation for form and content and recommend that it be accepted in partial fulfillment of the requirements for the degree of Doctor of Philosophy, with a major in Physics.

Joseph H. Macek, Major Professor

We have read this dissertation
and recommend its acceptance:

Predrag S. Krstic

Adolfo G. Eguiluz

Robert J. Harrison

Accepted for the Council:

Carolyn R. Hodges

Vice Provost and Dean of the Graduate School

(Original signatures are on file with official student records.)

Atomistic Simulations of the Fusion-Plasma Material Interface

A Dissertation

Presented for the

Doctor of Philosophy

Degree

The University of Tennessee, Knoxville

Mostafa Jon Dadras

May 2012

© by Mostafa Jon Dadras, 2012
All Rights Reserved.

This work is dedicated to my grandparents and to the Infinite, of which three of them are a part, and to Cori Mixon; who reminded me what it means to love and be loved.

Acknowledgements

I am thankful to all members of my committee. I am grateful to my major professor, Dr. Joe Macek, and especially to my research advisor, Dr. Predrag Krstic, without whose deep physical insight and seemingly infinite patience this work would not be possible.

I acknowledge support from the ORNL LDRD SEED program and the use of the super-computers: “Jaguar” of NCCS at ORNL and “Kraken” of NICS at UT.

Finally, I thank all of my friends and family for their patience and encouragement; in particular my mom, who started me out on this path and encouraged me to finish it, and my beautiful Pumpkin-face.

Sheer processing power is not a pixie dust that magically solves all your problems.

-Steven A. Pinker

*At quite uncertain times and places,
The atoms left their heavenly path,
And by fortuitous embraces,
Engendered all that being hath.
And though they seem to cling together,
And form "associations" here,
Yet, soon or late, they burst their tether,
And through the depths of space career.*

*So we who sat, oppressed with science,
As British asses, wise and grave,
Are now transformed to wild Red Lions,
As round our prey we ramp and rave.
Thus, by a swift metamorphosis,
Wisdom turns wit, and science joke,
Nonsense is incense to our noses,
For when Red Lions speak, they smoke.*

...

-James C. Maxwell, from *Molecular Evolution*

Abstract

A key issue for the successful performance of current and future fusion reactors is understanding chemical and physical processes at the Plasma Material Interface (PMI). The material surfaces may be bombarded by plasma particles in a range of impact energies (1 eV - a few keV) and kept at a range of temperatures (300 - 1000 K). The dominant processes at the PMI are reflection and retention of impacting particles and sputtering (chemical and physical). Sputtering leads to surface erosion and pollution of the plasma, both of which degrade reactor performance. Retention influences the recycling of the plasma, and in the case of tritium, raises the question of radioactive waste. PMI is a multi-scale problem, ranging from timescales of femtoseconds to years and spatial scales between Angstroms to meters. The main goal of this dissertation is to model PMI processes at the nanometer/nanosecond scale using atomistic Molecular Dynamic (MD) approaches. In particular, simulations have been done on mixed amorphous materials: hydrogenated, lithiated, and oxygenated carbon; bombarded by H isotopes using Classical Molecular Dynamics (CMD) and a Quantum-Classical Molecular Dynamics (QCMD) approach.

Contents

List of Tables	ix
List of Figures	x
1 Introduction and Motivation	1
2 Theoretical Methods	6
2.1 Classical Molecular Dynamics	8
2.1.1 Hydrocarbon Potentials (AI)REBO	9
2.1.2 Improved REBO	12
2.1.3 Towards a BOP for Li-C-H	16
2.2 Quantum-Classical Molecular Dynamics	20
2.2.1 Density-Functional Tight-Binding	22
2.2.2 Development of DFTB Parameters	29
3 Physical-Chemical Processes at the Plasma-Material Interface	33
3.1 Energy and Temperature dependence of Chemical sputtering of a-C:D surfaces bombarded by D	34
3.2 Sputtering Results from Refitted-REBO	45
3.3 Dynamics and Chemistry of Surfaces of Lithiated and Oxygenated Carbon, Bombarded by Deuterium	46
3.3.1 Isotopic Effects	57
3.3.2 Comparison with PW-DFT	61

4	Conclusions	63
	Bibliography	66
A		77
	Vita	82

List of Tables

2.1	Parameters for the attractive and repulsive pair terms of REBO and RREBO (in bold). Results from Kent et al. (2011).	14
2.2	Fitted and computed properties of the RREBO potential, table from Kent et al. (2011).	15
2.3	Parameters for the attractive and repulsive pair terms of the BOP. Note that we assume a single attractive potential, as is the case for C-H and H-H bonding, see Eq's 2.11 and 2.12.	17
2.4	List of partial charges calculated for a subset of small lithiated molecules, using GE to solve the EEM matrix.	21

List of Figures

1.1	Schematic of the NSTX reactor at PPPL and photograph of the inside of the reactor (the vacuum vessel) after a campaign. Images from Kugel (2010)	3
1.2	Schematic of the ITER reactor. Images from Organization (2010)	4
2.1	Plot showing the difference in short-distance behavior of REBO and ZBL, from Kent et al. (2011).	13
2.2	Comparison of the binding energies of the dimers Li ₂ , LiH, and LiC; computed from DFT (green circles) and the results of the BOP using lithium parameters from Table 2.2 (blue squares). Lines are meant only to guide the eye.	18
3.1	Renderings of a-C:D surface bombarded by D ₂ (C in yellow, H in white) and a-C:Li with D retained (C in black, Li in purple, H in white)	34
3.2	Comparison of carbon sputtering yields from simulations of Salonen et al. (2001) for plasma bombarding an a-C:T surface (triangles) with results of this work for a virgin a-C:D surface bombarded by 10 eV deuterium (squares). Error bars of the current results show the standard error obtained from one surface, the data from Salonen et al. (2001) show the standard error from 6 different surfaces. Figure from Dadras and Krstic (2011).	36

3.3	Comparison of sputtering yields for surfaces bombarded by 15 eV deuterium as a function of surface temperature. Experimental data of Mech et al. (1998) (hollow squares) and Balden and Roth (2000) (stars); Dadras and Krstic (2011) (filled circles) with error bars representing standard error obtained from 6 different surfaces.	37
3.4	3D plot of the carbon sputtering yield as a function of both surface temperature and energy of the impacting particle, compared to experimental data from Balden and Roth (2000) (hollow stars); figure from Dadras and Krstic (2011)	41
3.5	Total carbon sputtering yields before (hollow circles) and after (filled circles) "super-heating," compared to experiments (filled stars) of Balden and Roth (2000); for various impact energies (a - c). Methane and acetylene sputtering yields before (hollow symbols) and after (filled symbols) super-heating, for various energies (d - f). Figure from Dadras and Krstic (2011).	42
3.6	Reduction of deuterium from super-heating. Shown are fraction a) D/D_0 at various impact energies and b) D/C , after and prior to forced deuterium release. Measurements of the thermally induced release rate from Doerner et al. (2009) is shown by X symbols. Figure from Dadras and Krstic (2011).	43
3.7	Moiety fraction in the whole cell between final, i.e. over-heated, (b) and initial "virgin" (a) surfaces.	44
3.8	Change of 3-fold and 4-fold moieties as functions of T for the cumulatively bombarded surfaces, for 15 (a) and 20 eV (b) impact energy. The change of moieties is even more pronounced than in the "virgin" case, but do not result in a peak of the sputtering yields with temperature.	44

3.9	Sputtering yields obtained by bombardment of a-C:D by D at various impact energies: a) $CD_3 + CD_4$ of CMD and experimental results on CD_4 . b) C_2D_2 of CMD with C_2D_y of experiments. c) total carbon yield C_xD_y for $x \leq 4$ and CD_x , C_2D_2 , C_2D_4 , C_2D_6 , C_3D_6 and C_3D_8 from experiments of Meyer et al. (2011), figure from Kent et al. (2011).	46
3.10	XPS measurement of oxygen diagnostics at 200 eV and 50 eV impact deuterium. The control group at thermal energies is also shown; figure from Taylor and Allain (2011).	50
3.11	Cumulative surface concentration of O, Li and C upon deuterium bombardment	50
3.12	Distribution of charges in the systems (a - d) and normalized cumulative distributions of charges (e - h).	52
3.13	Distributions of nearest neighbors to retained D (a - d) and their cumulative distributions (e - h).	53
3.14	Distribution of the final kinetic energies of the retained D (a), and their normalized cumulative distributions (b).	54
3.15	The partial charge distributions for a “cumulative” D case.	55
3.16	The nearest neighbor distributions for a “cumulative” D case.	55
3.17	a) Retention and reflection probabilities of impact D, and b) total and C sputtering yields of the various cases. A: a-C; B: 20% Li; C: 20% Li and O; D: 20% O in C.	56
3.18	Penetration depth of deuterium into deuterated carbon of 2 g/cm ³ , for various impact energies of D. Figure from Krstic et al. (2007b).	58
3.19	Penetration distributions of a) D and b) H into LiCO mixture. Interface of the surface with vacuum prior to bombardment is presented by vertical dashed line perpendicularly to the interface. Figure from Krstic et al. (2011).	58
3.20	Charge distributions of a) D and b) H, as well as of Li, C and O upon the retention process. Figure from Krstic et al. (2011).	59

3.21	Sputtering yields (in %) of the LiCO surface by a) H impact and b) D impact. Figure from Krstic et al. (2011).	60
3.22	Energy distribution of the reflected (a) hydrogen, (b) deuterium atoms. Solid lines: Boltzmann distribution fit. Figure from Krstic et al. (2011).	61
3.23	Double-layer graphitic slab with Li and H atoms. Figure from Krstic et al. (2011).	62
3.24	Charges of Li and H atoms for various positions of the H atom. AD: increasing distance LiH. E: corresponding to Li intercalated between two planes. Figure from Krstic et al. (2011).	62
A.1	Distribution of charges in the systems, when using only the s-basis in Li.	78
A.2	Nearest neighbors distributions to impacting and stuck D, when using only the s-basis in Li.	78
A.3	Comparison of penetration depth profiles between (a - d) using only the s-basis in Li and (e - h) using the s-p basis.	79
A.4	Comparison of binding energy distributions between (a - d) using only the s-basis in Li and (e - h) using the s-p basis.	80
A.5	Comparison of retention and reflection probabilities of impact D a), and total and C sputtering yields of the various cases A: a-C; B: 20% Li; C: 20% Li and O; D: 20% O in carbon b); using the s and s-p bases.	81
A.6	a) penetration depth and b) binding energy for the “cumulative” surface, using the s-p basis in Li.	81

Chapter 1

Introduction and Motivation

The growing human population coupled with the improving quality of life for all people, requires meeting very demanding global energy needs while minimizing the green house effect and other pollutants that can lead to climate and other negative environmental changes. A promising line of research is in developing and improving the already well-established fission reactors. There are, however, a few issues of serious concern for fission reactors: One of these is the requirement of storing radioactive waste for time periods on the order of 10,000 years, another issue is controlling runaway reactions that can cause meltdowns leading to environmental contamination. Finally, there are the issues of the availability of uranium ore as well as producing the needed fissile fuel, requiring the construction of large enrichment plants which brings up concerns of national security.

Another option for mass energy production is nuclear fusion. Unlike fission, where only 0.1% of the mass is converted into energy in the nuclear reaction, close to 1% of the mass is converted into energy in the fusion reaction of deuterium and tritium; fusion also has an advantage over fission in not producing large quantities of radioactive waste and that an operational malfunction will only lead to rapid shutdown of the fusion process. Another attractive feature of fusion is also the abundance of the required fuel (deuterium and tritium). About 0.015% of the

hydrogen in sea water is deuterium. Tritium is bred from interactions of energetic neutrons with lithium. By mole fraction, lithium is about 100 times more abundant than uranium in the earth's crust.

The most developed avenue of research toward the commercialization of fusion power is magnetic confinement (in so called tokamaks), where very strong magnetic fields (on the order of a few Tesla) in a donut-like formation are used to compress and heat plasmas of D and T to induce fusion. As of now plans are in development to have a magnetic confinement device to demonstrate commercial feasibility before the year 2032 (ITER/DEMO). Since walls and other solid components of the reactors are exposed to huge power fluxes ($\geq 10 \text{ MW/m}^2$) carried by the plasma particles and neutrons, a key requirement for the success of any such device is to qualify and quantify the erosion rates of wall materials and components, as well as reflection and retention of H and He ions/atoms and other plasma particles bombarding the surfaces.

This dissertation focuses on a few materials in two large fusion reactor projects in development: The first is the National Spherical Torus Experiment with a Liquid Lithium Divertor (NSTX-LLD). NSTX is a spherical tokamak at the Princeton Plasma Physics Laboratory (PPPL). The reason for the spherical design is that previous magneto-hydrodynamic studies have shown that the plasma pressures required to maintain fusion can be achieved with a smaller magnetic field strength than in the more traditional torus shaped device. The central magnet is about 4 m tall; the first wall components are primarily graphite tiles, used for their excellent thermal and mechanical properties. Liquid Lithium (LLi) as divertor material has attracted attention because it is self-healing to the damages caused by plasma particle irradiation, it has high heat removal capabilities, and recycling of hydrogen isotopes (see e.g. [Evtikhin et al. \(2002\)](#)).

The divertor region, where the magnetic field lines end (and thus where there is the largest flux of impacting particles), at the bottom of the reactor, has a layer of lithium on a molybdenum substrate, surrounded by graphite tiles, where lithium

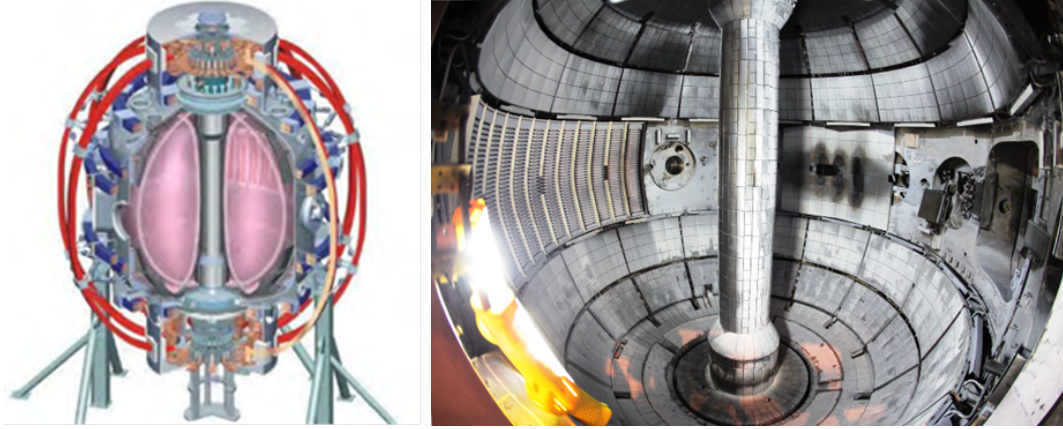


Figure 1.1: Schematic of the NSTX reactor at PPPL and photograph of the inside of the reactor (the vacuum vessel) after a campaign. Images from [Kugel \(2010\)](#)

also deposits. Since lithium is an excellent oxygen getter (due to the vastly different electronegativities of the atoms, 0.98 for Li and 3.44 for O on the Pauling scale), it is necessary to consider oxygen, always present in small quantities in commercial lithium and in the reactor vessel in the form of water, to accurately model chemical/physical processes of interest. Thus, one of our interests concerns mixed materials containing Li-C-O-H, at temperatures in the range of 300 K. Figure 1.1 shows an artist's rendering of the device in operation, and also shows a photograph of the NSTX spherical device depicting the carbon wall tiles coated in lithium.

The other reactor is the ITER (originally meaning the International Thermonuclear Experimental Reactor), Latin for "The Way," which has recently broken ground in Cadarache, France. It follows a standard toroidal design. The vacuum vessel will have an external diameter of about 19.5 m, an internal diameter of about 6.5 m, and be close to 11.5 m in height. Figure 1.2 shows a cut-away schematic of ITER reactor and its various components. The first wall material for ITER will be beryllium tiles; beryllium is also a good oxygen getter. The divertor will be made of Carbon Fiber-reinforced carbon Composite (CFC). The divertor dome is made of tungsten. Also, it is planned that tungsten and the tungsten-deposited layers on carbon will eventually replace all walls of the DEMOnstration Power Plant (DEMO); the first reactor which

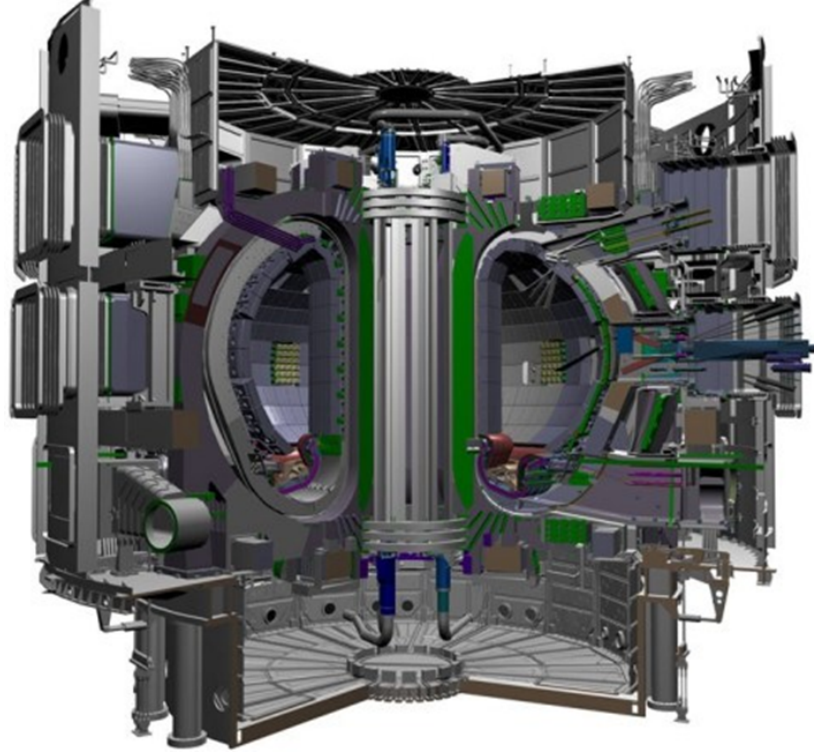


Figure 1.2: Schematic of the ITER reactor. Images from [Organization \(2010\)](#)

will perform energy conversion. Tungsten also has good thermal and mechanical properties, as well as a lower erosion rate as compared with carbon; however, it is noted that W is a high Z material implying that many charge states can be populated and thus more energy can be leached from the plasma when tungsten does get sputtered. While ITER will be pulsed experimental machine, with the divertor cooled to nearly room temperature, DEMO will perform continuously, with walls at about 1000 K (to induce the energy conversion), which sets extreme conditions for the DEMO materials. In this regard, research is increasingly focused on surfaces of mixed W-C-H-He materials.

Finally, the temperature of the plasma surrounding the walls, the so called Edge, has a temperature significantly lower than in the core. Thus, a typical range of the energies for the divertor plasma particles is 1 - 50 eV, concentrations of both ions and neutrals is about 10^{15} cm^{-2} . The products from the fusion reaction $D + T \rightarrow \alpha(3.5\text{MeV}) + n(14.1\text{MeV})$, in particular neutrons, will penetrate into all wall

components causing dislocations and damages in the surfaces. Occasional fluxes of high energy ions during the so called plasma disruptions and Edge Localized Modes (ELMs) also cause damage to the bulk material, deep below the interface.

Traditionally the Plasma Material Interface (PMI) was studied in a trial and error fashion, by refitting the walls of tokamak devices with different materials and design components; this method can no longer be followed in future fusion reactors as it is prohibitively slow and costly (with surfaces of hundreds of square meters). Our approach instead is the bottom-up method. Hence, the goal of this dissertation will be to accurately model the PMI at the nano-scale by modeling processes at the atomistic level; thus building the scientific foundation for studies at realistic reactor space and time scales. Plasma-Surface or Beam-Surface Interactions (PSI) offer a window into the environment at the plasma edge in a reactor. The range of techniques spans several orders of magnitude in space and energy of impacting particles. For example, for bulk properties (≥ 50 nm) of importance to higher energy impacts (ranging from about 100 eV to 1 keV) experiments using Rutherford backscattering and elastic recoil detection can probe this region of phase space; computational models may use Monte-Carlo techniques and diffusion and transport codes. While at the level of about 1 - 5 nm (impact energies of about 1 - 100 eV) experiments employing low-energy ion scattering and X-ray Photoelectron Spectroscopy (XPS) coupled with surface models using Quantum and/or Classical Molecular Dynamics (Q/CMD) and Density Functional Theory (DFT) give insight into the physics at this scale. We are concerned with modeling the PMI at the more fundamental level and thus employ the methods of QCMD to this end. In the next chapter we give a brief overview of the various theoretical methods at our disposal and developments we have made and intend to make in future research. Following this we discuss the chemical and physical processes of interest for PMI applicable to the two reactors mentioned above. In the final chapter we draw conclusions and suggest future work.

Chapter 2

Theoretical Methods

The various physical and chemical processes relevant to the Plasma Material Interface (PMI) take place at different length and time scales. At the length-scales of Angstroms to tens of nanometers, with time-scales between fractions of a picosecond to about a nanosecond, and (since these time scales are determined by the impact particle's energy) low impact energies up to a few tens of eV; material damage production, particle cascades, and chemical sputtering are the dominant reactions. Atomistic simulations employing classical and quantum-classical MD, are appropriate to simulate the dynamics of these reactions, and are the subject of this work. At length-scales ranging from sub-micron to about 1 mm, dislocation and point-defect mobility and reactions as well as bubble formation and physical sputtering are the dominant physical processes. These reactions are studied using methods of discrete dislocation dynamics and Kinetic Monte-Carlo (KMC). At large length scales (from about 1 mm to several meters) and long time-scales (several seconds to years) issues of material swelling and changes to the macroscopic mechanical properties are important; theoretical methods employed use reaction rate and constitutive equations.

Besides low energy interactions the results of atomistic simulations (e.g. sputtering rates, diffusion coefficients, etc.) can be used as inputs for simulations of larger scale effects (e.g. to parameterize rate equations). Hence the small scale simulations have a

fundamental status. We employ the methods of classical and quantum-classical MD to model physical/chemical processes at the PMI; we fit interatomic potential parameters to data of small reference molecules and clusters from DFT and experiments.

The dynamics of a system of particles are governed by solving Newton’s laws of motion in a particular potential (V_{tot}). To accomplish this numerically, various algorithms can be used. Both of our methods employ the Verlet Algorithm, in which the force on the i^{th} atom is given by:

$$F_i = m_i \ddot{r}_i = -\frac{\partial V_{tot}}{\partial r_i} \quad (2.1)$$

$$r_i(t + \delta t) = 2r_i(t) - r_i(t - \delta t) + \frac{\delta t^2}{m_i} F_i + \dots \quad (2.2)$$

$$\dot{r}_i(t) = \frac{1}{2\delta t} (r_i(t + \delta t) - r_i(t - \delta t)) + \dots \quad (2.3)$$

$$\ddot{r}_i(t) = \frac{1}{\delta t^2} (r_i(t + \delta t) - 2r_i(t) + r_i(t - \delta t)) + \dots \quad (2.4)$$

Thus the energy and forces of the system are updated after each time-step (δt) as the configuration of the atoms changes. To control the temperature of the system in our Classical MD (CMD) studies a Langevin thermostat is used; this is ideal to smoothly remove or add heat to the system. While for our Quantum-Classical MD (QCMD) approach a Nose-Hoover thermostat is used to quickly add or remove energy as the time-scales are shorter for this method. Hence, classically the equations of motion become:

$$m_i \ddot{r}_i = -\frac{\partial V_{tot}}{\partial r_i} - \gamma m_i \dot{r}_i + \sqrt{2\gamma k_b T m_i} R(t) \quad (2.5)$$

where γ is a damping factor, k_b is Boltzmann’s constant, and $R(t)$ is a time-dependent Gaussian process, and energy is adiabatically removed from the system to keep the

average kinetic energy of the atoms near a central value. In our QCMD approach, for a thermostatted system, equations of motion for the atoms are:

$$m_i \ddot{r}_i = -\frac{\partial V_{tot}}{\partial r_i} - \xi m_i \dot{r}_i \quad (2.6)$$

$$\dot{\xi} = -\frac{k_b N_{dof}}{Q} T(t) \left(\frac{g T_0}{N_{dof} T(t)} - 1 \right); \quad (2.7)$$

where Q is a fictitious *inertial* term that determines the coupling to the heat bath, g is set equal to the number of degrees of freedom (N_{dof}) in the Nose-Hoover formalism— for more information on thermostats in MD see e.g. [Adelman and Doll \(1976\)](#); [Hoover \(1985\)](#).

The primary difference in our CMD and QCMD approaches is in the determination of the interatomic potential energies, and thus the forces on atoms. Hence the subject of discussion in the rest of this chapter is focused on analytical Bond Order Potentials (BOP) used in CMD and determination of parameters used for the energy expression in our QCMD method (Density Functional Tight-Binding, DFTB).

2.1 Classical Molecular Dynamics

Classical Molecular Dynamics (CMD) relies on the predefined classical MD potential. Simulations of the PMI can only be as realistic as the quality of this potential. Bond-Order Potentials (BOPs) have shown to be useful in modeling chemical reactivity (important at the low energy scales of interest). The classical BOP was first conceived, in its modern form, by Tersoff and Abell ([Tersoff \(1988\)](#); [Abell \(1985\)](#)), in those works the authors used semi-classical reasoning to create empirical potentials that are written as a sum of attractive and repulsive components scaled by an environment-dependent (i.e. bond order) term; the attractive and repulsive parts have a Morse-type form:

$$V_m(r) \propto D_e \left(e^{-2a(r-R^e)} - 2e^{-a(r-R^e)} \right), \quad (2.8)$$

where D_e is the well depth, R^e is the equilibrium distance, and $2D_e a^2$ is the force constant. Brenner in (Brenner (1990)) further developed this Morse-type potential for hydrocarbons, adding a correction to the BO term. Finally, Brenner et al. (2002) made further improvements to the hydrocarbon potential expanding the analytic intramolecular expression; this Reactive Empirical Bond Order (REBO) potential is the base of our CMD studies and so it is instructive to go through a somewhat detailed description.

2.1.1 Hydrocarbon Potentials (AI)REBO

Yielding to arguments from Brenner et al. (2002), the binding energy (E_b) in a molecule is written as a sum over nearest neighbor atoms:

$$E_b = \sum_i \sum_{j>i} [V^R(r_{ij}) - \bar{b}_{ij} V^A(r_{ij})]. \quad (2.9)$$

Here

$$\bar{b}_{ij} = \frac{1}{2} [b_{ij}^{\sigma-\pi} + b_{ji}^{\sigma-\pi}] + \Pi_{ij}^{RC} + b_{ij}^{DH}, \quad (2.10)$$

$$V^R(r) = f^c(r)(1 + Q/r)Ae^{-\alpha r}, \quad (2.11)$$

and

$$V^A(r) = f^c(r) \sum_{n=1,3} B_n e^{-\beta_n r}. \quad (2.12)$$

Using the symmetrized function (i.e. \bar{b}_{ij}) allows for accurate modeling of bond conjugation by allowing for the total energy to not just be divided into the sum of

site energies (i.e. non-local effects are included). The $b_{ij}^{\sigma-\pi}$ term takes into account local coordination and bond angles between atom i and atom j , and is given as:

$$b_{ij}^{\sigma-\pi} = \left(1 + \sum_{k \neq i, j} f_{ik}^c(r_{ik}) G(\cos(\theta_{ijk})) e^{\lambda_{ijk}} + P_{ij}(N_i^C, N_i^H) \right)^{-1/2} \quad (2.13)$$

$$G(\cos(\theta_{ijk})) = 1 + \frac{c^2}{d^2} - \frac{c^2}{d^2 + (h - \cos \theta_{ijk})^2} \quad (2.14)$$

The second term ($G(\cos(\theta_{ijk}))$) takes into account the angular dependence of the binding energy, by imposing a penalty on bonds that are too close to each other; it is noted that if the central atom is a carbon then the function also depends on the local coordination number, given as a sum of the separate carbon and hydrogen coordination numbers. The $e^{\lambda_{ijk}}$ term is incorporated to stabilize the potential energy surface for detachment of hydrogen from hydrocarbons. Finally, P_{ij} is a bicubic spline that depends also on the carbon and hydrogen coordination numbers, that are neighbors of the i^{th} atom. There is a similar expression for the $b_{ji}^{\sigma-\pi}$ term, but with i and j transposed.

The cut-off function $f^c(r)$, in equations 2.11 - 2.13, limits the range of covalent bonding, $f^c(r) = 1$ for nearest neighbor interactions and zero for all other distances. This approach was inspired by [Tersoff \(1988\)](#); a switching function is employed with a range given by (D_{ij}^{min} and D_{ij}^{max}). Hence, the cut-off function is:

$$f^c(r) = \begin{cases} 1 & r < D^{min} \\ \frac{1}{2} \left(1 + \cos \left(\frac{r - D^{min}}{D^{min} + D^{max}} \right) \right) & D^{min} < r < D^{max} \\ 0 & r > D^{max} \end{cases} \quad (2.15)$$

The Π_{ij}^{RC} term in equation 2.10 depends on if the bond between atom i and atom j has a radical character and is part of a conjugated system. It is represented by a tricubic spline in the variables of the coordination numbers of atoms i and j , and the local measure of conjugacy in the $i - j$ bond; this is based on the coordination number of the i^{th} (j^{th}) atom and its neighbors excluding the j^{th} (i^{th}) atom. Finally

the term, b_{ij}^{DH} , applies a penalty for rotation around multiple bonds (i.e. a torsional barrier). It is also represented by a similar tricubic spline, as with Π_{ij}^{RC} , but is scaled by weighted sums of all torsional barriers between atoms bonded to atoms i and j , and their neighbors.

This potential is expanded to the Adaptive Intermolecular REBO (AIREBO) potential by [Stuart et al. \(2000\)](#), with the inclusion of intermolecular forces, i.e. dispersion and intermolecular repulsion as well as torsion. The dispersion and repulsion were modeled using the Lennard-Jones 12-6 potential given by

$$V_{ij}^{LJ}(r_{ij}) = 4\epsilon_{ij} \left(\left(\frac{\sigma_{ij}}{r_{ij}} \right)^{12} - \left(\frac{\sigma_{ij}}{r_{ij}} \right)^6 \right). \quad (2.16)$$

Here ϵ is well-depth of the pair potential and σ is the distance where the potential goes to zero. This interatomic potential is cut-off for distances larger than 10 Å, and is also zero for atom pairs that are first or second nearest neighbors. The torsional interaction is used to model the dependence of the binding energy on the dihedral angle (ω) for single bonds, rather than multiple bonds like b_{ij}^{DH} , and is represented in the following way:

$$V_{ij}^{tors}(\omega_{kijl}) = \beta_{kijl} \left(\frac{256}{405} \cos^{10} \left(\frac{\omega_{kijl}}{2} \right) - \frac{1}{10} \right), \quad (2.17)$$

where β is the barrier height; the potential is then scaled by the bond-weights* that contribute to the dihedral angle; this guarantees that the torsional energy from a particular dihedral angle is smoothly removed when any of the constituent bonds are broken.

For further details on (AI)REBO and its development, as well as a full listing of its parameters, we refer the reader to ([Tersoff \(1988\)](#); [Abell \(1985\)](#); [Brenner et al. \(2002\)](#); [Stuart et al. \(2000\)](#)). In the next subsection we discuss our recent improvements to REBO, in particular for short-distance interactions (i.e. for atomic collisions up to energies on the order of 1 keV, well beyond the realm of most chemical phenomena).

*The bond weight is a switching function that depends on the distance between a pair of atoms.

2.1.2 Improved REBO

The REBO potentials are created by fitting selected bonding and non-bonding terms to a database of solid-state and chemical data. These data include (see [Brenner et al. \(2002\)](#); [Stuart et al. \(2000\)](#)) the lattice constant and cohesive energy of carbon graphite and diamond, and the carbon-carbon and carbon-hydrogen bond lengths, force constants, and bonding energies for a range of lighter hydrocarbons (e.g. methane, acetylene, cyclohexane). Consequently, although the energetics of low energy and low temperature interactions are well-described, it is not so for medium energy and close encounter collisions, greater than a few tens of eV.

In [Kent et al. \(2011\)](#) we refitted the (AI)REBO potentials to a revised database of lightweight hydrocarbons and solid-state carbon systems, and also by incorporating the universal repulsive Ziegler, Biersack, and Littmark (ZBL) potential ([Ziegler et al. \(1985\)](#)) at short range—namely, at high impact energies where binary repulsive interactions dominate. This short-distance part of the REBO potentials was previously not fitted correctly because of the lack of interest of the authors for higher than thermal impact energies. The refitted potential therefore captures the existing accuracy of the REBO form while reproducing the inner core ionic repulsion for higher energy collisions. All target properties, as opposed to the few-parameters and few-properties originally used by [Brenner \(1990\)](#) and [Brenner et al. \(2002\)](#), have been simultaneously fit.

The ZBL potential is given as a weighted sum of exponentials:

$$V_{ZBL}(r) = \frac{1}{4\pi\epsilon_0} \frac{Z_1 Z_2}{r} \phi(x), \quad (2.18)$$

where

$$\phi(x) = 0.1818e^{-3.2x} + 0.5099e^{-0.9423x} + 0.2802e^{-0.4029x} + 0.02872e^{-0.2016x}, \quad (2.19)$$

and

$$x = \frac{r(Z_1^{0.23} + Z_2^{0.23})}{0.8854a_0}. \quad (2.20)$$

Here, the Z 's are the nuclear charges of the interacting pair and $a_0 = 0.529 \text{ \AA}$ is the Bohr radius. To incorporate the ZBL potential the existing repulsive potential was smoothly interpolated to ZBL over a small energy range, between 10 and 30 eV.

Fitting the potential was accomplished by a weighted least squared deviation fitting procedure using the Levenberg-Marquardt method. This procedure does not guarantee finding of the global minimum, and further improvements of the fits might be possible. The original REBO fit was found to be accurate. Still, there were notable improvements for some of the C-C and C-H terms. The hydrogen potential (H-H) was left unchanged.

Figure 2.1 illustrates different components of the potentials. The prior REBO fit is clearly too repulsive, out pacing the ZBL potential at short range. The new potential, Refitted-REBO (RREBO), retains the existing shape of the REBO potential in the bonding region, preserving its quality for low energy interactions, but now interpolates to the ZBL interaction at high energies, indicating that this potential may be more accurate for energy ranges of interest for PMI. Table 2.1 shows the refitted REBO parameters for the attractive and repulsive pair terms.

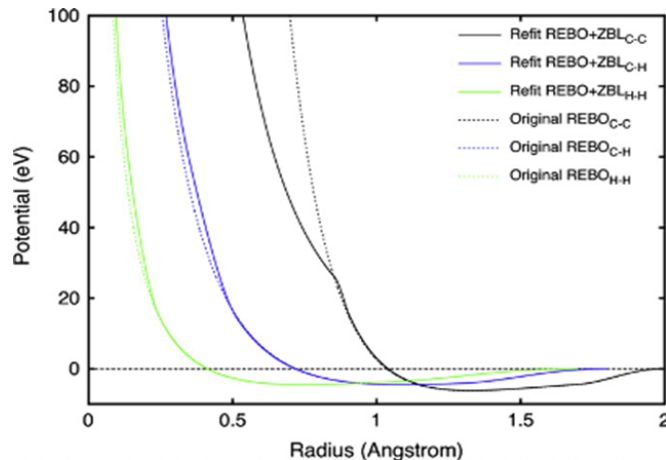


Figure 2.1: Plot showing the difference in short-distance behavior of REBO and ZBL, from Kent et al. (2011).

In Table 2.2 we list properties calculated with refitted REBO for a variety of systems. Bond lengths are reproduced typically to within a few hundredths of an Angstrom and binding energies to within one tenth of an eV; the largest error in binding is for the benzene molecule, at about 0.7 eV, i.e. 1%. The accuracy of the fit validates the REBO potential form for the fitted species. The high accuracy also indicates the ZBL term has not affected low energy properties. We note that with the current form of the potential, improvements to any individual fitted property could be made at the expense of a global worsening of other properties. More significant improvements in accuracy might be possible by fitting, e.g., reaction barriers specific to plasma applications. For more details on RREBO we refer the reader to [Kent et al. \(2011\)](#); in chapter 3 sputtering simulations using this improved REBO potential are presented, showing a somewhat improved comparison with experimental observables.

Table 2.1: Parameters for the attractive and repulsive pair terms of REBO and RREBO (in bold). Results from [Kent et al. \(2011\)](#).

	(C-C)	(C-H)	(H-H)
A	10,953.544	149.941	31.673
	10,678.932	147.666	
α	4.747	4.103	3.536
B_1	12,388.792	32.355	28.23
	12,113.462	31.911	
β_1	4.721	1.435	1.708
		1.426	
B_2	17.568	0	0
	57.479		
β_2	1.433	0	0
B_3	30.715	0	0
	-6.345	0	0
β_3	1.383	0	0
Q	0.314	0.341	0.37
	0.327		

Table 2.2: Fitted and computed properties of the RREBO potential, table from Kent et al. (2011).

Species	Goal Atm. En. (eV)	Fit Atm. En. (eV)	Goal $R_{C-C}(\text{Å})$	Fit $R_{C-C}(\text{Å})$	Goal $R_{C-H}(\text{Å})$	Fit $R_{C-H}(\text{Å})$
Methane	-18.19	-18.19			1.09	1.09
Ethyne	-17.57	-17.43	1.20	1.21	1.09	1.09
Ethene	-24.41	-24.47	1.33	1.31	1.09	1.09
Ethane	-30.84	-30.82	1.54	1.54	1.09	1.09
Propyne	-30.31	-30.14				
Propene	-37.30	-37.42				
Propane	-43.59	-43.54				
Benzene	-59.29	-59.98	1.39	1.37	1.09	1.09
Cyclohexane	-76.45	-76.32	1.54	1.54	1.09	1.09
Ethylene	-24.41	-24.47				
Acetylene	-17.57	-17.43				
CH2	-8.47	-8.47				
CH3	-13.375	-13.377				
C2H	-11.57	-11.49				
Diamond	-7.36	-7.32	1.54	1.54		
Graphite	-7.40	-7.46	1.42	1.40		

2.1.3 Towards a BOP for Li-C-H

Lithium is unique among the mentioned materials as it has a very small electronegativity ($\chi = 0.98$, Pauling scale); carbon, hydrogen, and oxygen have χ 's of 2.55, 2.20, and 3.44; respectively, which is why lithium is such an excellent oxygen getter. This fact necessitates the inclusion of nonbonding Coulomb interactions arising between partially charged atoms, in addition to the covalent interactions described with the potentials of the (AI)REBO type.

Starting with the form of the REBO potential as given by [Brenner et al. \(2002\)](#), including the short-range ZBL repulsion and neglecting the effects of LJ, torsion, dihedral angles, and radical bonding; we have developed a Bond-Order Potential (BOP) for the Li-C-H system. We do not try to model the *bcc* phase of lithium; i.e. we do not attempt to include second nearest neighbor interactions that may be required to accurately model lithium metal at standard temperature and pressure, as was done for tungsten by [Juslin et al. \(2005\)](#). We argue that this is not required as a lithium divertor will be in liquid (amorphous) rather than solid (crystal) form under operating conditions in a reactor (thus in a phase where the second nearest neighbors are significantly further away than the first nearest neighbors). More importantly, we are primarily interested in modeling chemical/physical reactions involving mixed amorphous Li-C-H surfaces that are predominantly carbon. In fact, all surfaces exposed for long times to the fusion plasma take an amorphous form. We argue that in such a system the Coulomb interactions between the partial charges—induced from the Electronegativity Equalization Method (EEM)—coupled with our BOP will take into account essential material properties relevant for the study of the PMI; this hypothesis can be tested against experimental data (e.g. on sputtering and hydrogen retention).

Table 2.3 shows a list of the parameters, using the same fitting scheme as for hydrocarbons, of the attractive and repulsive pair potentials; again, the angular parameters (from equations 2.13 and 2.14) were set to those of hydrogen as a first

Table 2.3: Parameters for the attractive and repulsive pair terms of the BOP. Note that we assume a single attractive potential, as is the case for C-H and H-H bonding, see Eq’s 2.11 and 2.12.

	(C-Li)	(H-Li)	(Li-Li)
A	-122.1392	-61.7395	-1.2242
α	2.9174	1.4796	0.4154
B_1	21.0963	3.1725	3.2945
β_1	0.829	0.6666	0.2388
Q	-6.7493	-1.321	-8.0102

approximation. Figure 2.2 shows a comparison between the calculated energies of dimers from a DFT (B3LYP/6-31G**) calculation and our BOP near the DFT equilibrium position; hence these show the binary BOPs between Li-C, Li-H, and Li-Li near the minimum. Discrepancies exist due to the fact that we are fitting to small clusters as well as dimers, and that we cut the function off to keep the coordination number of carbon atoms within a reasonable range.

A key feature in our potential energy expression for the Li-C-H system is the inclusion of the Coulomb term, hence:

$$V_{tot} = V_{BO+ZBL} + V_{Coul}, \quad (2.21)$$

where

$$V_{Coul} = C \frac{q_i q_j}{[r_{ij}^3 + (1/\gamma_{ij})^3]^{1/3}}, \quad (2.22)$$

with C and γ_{ij} are parameters to be fitted. This soft-core form of the Coulomb potential was argued for by van Duin et. al. (van Duin et al. (2001)) to adjust for orbital overlap between atom pairs; and was employed by Han et. al. (Han et al. (2005)), in their own attempt at developing classical potentials of the Li-C-H system.

The partial charges are determined from the Electronegativity Equilibration Method (EEM); as such, it is instructive to summarize this method. Following arguments from Mortier et. al. (Mortier et al. (1986)), EEM is a semi-empirical

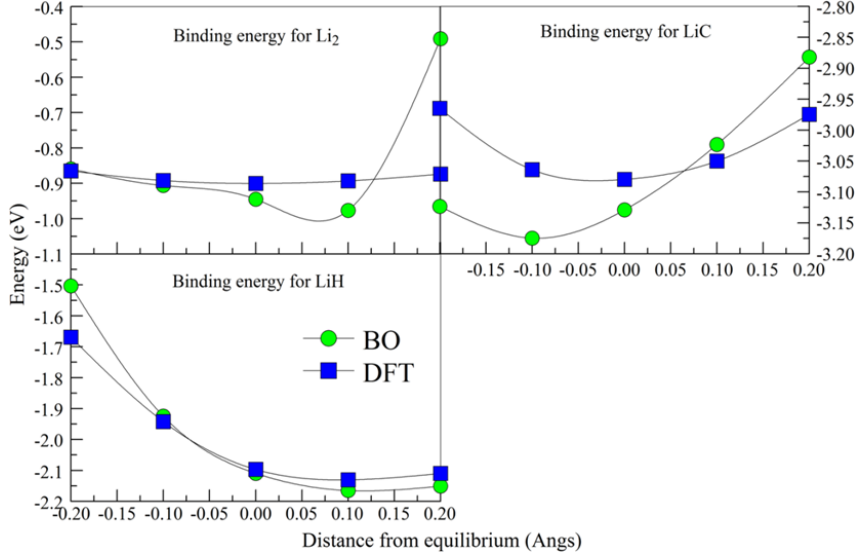


Figure 2.2: Comparison of the binding energies of the dimers Li₂, LiH, and LiC; computed from DFT (green circles) and the results of the BOP using lithium parameters from Table 2.2 (blue squares). Lines are meant only to guide the eye.

approach to DFT. The total energy (E) of a molecule can be expanded to 2^{nd} order in terms of the electron density or equivalently in terms of electron number (N):

$$E_{tot} = E^0 + \left(\frac{\partial E}{\partial N} \right)_0 \Delta N + \frac{1}{2} \left(\frac{\partial^2 E}{\partial N^2} \right)_0 \Delta N^2 + \dots \quad (2.23)$$

Here zeroth-order terms represent properties that belong to the neutral atoms. Then by taking a partial derivative with respect to N we define the electronegativity (χ), the chemical potential (μ), and the chemical hardness (η) in the following way:

$$\chi = -\mu = -\frac{\partial E}{\partial N}, \quad (2.24)$$

$$\eta = \frac{1}{2} \frac{\partial^2 E}{\partial N^2}. \quad (2.25)$$

Noting that the total energy depends on the kinetic energy, the nuclear-nuclear repulsion, the electron-electron repulsion, and the nuclear-electron attraction; and

generalizing our equation to represent atoms with differing electron counts (N_α, N_β, \dots), we write the energy of a molecule as:

$$E_{tot} = \sum_{\alpha} E_{\alpha}^* + \mu_{\alpha}^* \Delta N_{\alpha} + \eta_{\alpha}^* (\Delta N_{\alpha})^2 - N_{\alpha} \sum_{\beta \neq \alpha} \frac{Z_{\beta}}{R_{\alpha\beta}} + \frac{N_{\alpha}}{2} \sum_{\beta \neq \alpha} \frac{N_{\beta}}{R_{\alpha\beta}} + \frac{1}{2} \sum_{\beta \neq \alpha} \frac{Z_{\alpha} Z_{\beta}}{R_{\alpha\beta}} \quad (2.26)$$

Z_{α} is the nuclear charge of the α^{th} atom. And $Y^* = Y_0 + \Delta Y$, for $Y = E, \mu, \eta$; and ΔY is the change in the corresponding quantity.

By taking the partial derivative with respect to N_{α} we find

$$\chi_{\alpha} = \chi_{\alpha}^* + 2\eta_{\alpha}^* q_{\alpha} + 14.4 \sum_{\beta \neq \alpha} \frac{Z_{\beta} - N_{\beta}}{R_{\alpha\beta}}. \quad (2.27)$$

The term $Z_{\alpha} - N_{\alpha} = q_{\alpha}$ is the induced partial charge and the number 14.4 is a conversion factor (see [Njo et al. \(1998\)](#)). If the molecule has a unique chemical potential as a whole then this necessitates the EEM, implying that

$$\chi_{\alpha} = \chi_{\beta} = \chi_{\gamma} = \dots = \bar{\chi} \quad (2.28)$$

for each atom $\alpha, \beta, \gamma, \dots$. The total charge (Q) of the molecule is just the sum of all the partial charges; hence the following matrix equation must be solved:

$$\begin{pmatrix} 2\eta_1^* & 1/R_{12} & \cdots & -1 \\ 1/R_{21} & 2\eta_2^* & \cdots & -1 \\ \vdots & \vdots & \ddots & \vdots \\ 1 & 1 & \cdots & 0 \end{pmatrix} \begin{pmatrix} q_1 \\ q_2 \\ \vdots \\ \bar{\chi} \end{pmatrix} = \begin{pmatrix} -\chi_1^* \\ -\chi_2^* \\ \vdots \\ Q \end{pmatrix}. \quad (2.29)$$

The method of Gaussian Elimination (GE) is used to solve the EEM matrix, from [Yang \(2010\)](#). Optimized values of η^* and χ^* as given by [Mortier et al. \(1986\)](#) were used, and values for lithium were extrapolated by making a linear fit to data between

Han et al. (2005) and Mortier et al. (1986). Table 2.4 shows results for the EEM charges for a training set of molecules that were also used to fit the BO parameters shown in Table 2.3. Results in Table 2.4 show the EEM charges to be in reasonable agreement with the DFT Mulliken charges.

It is noted that this classical Li-C-H potential has not yet been tested against experiments. Also, in order to model periodic systems (i.e. a surface) we have simply enforced a long-distance cut-off (10 Å) for the Coulomb interaction. Beyond this, lithium is an excellent oxygen getter and, as will be demonstrated in the next chapter, oxygen is a key player in the hydrogen chemistry in mixed amorphous materials of Li-C-O bombarded by H; this would require the development of a complete Li-C-O-H BOP. The need to recalculate atomic charges with EEM in each time step, increases the calculation time beyond the practicality obtained by CMD. A more physically motivated (and therefore potentially more accurate) quantum-classical method has been developed, with parameters for the Li-C-O-H system computed for this approximate quantum-mechanical approach (SCC-DFTB). This method allows systems under study to have a proper electron count, rather than an artificial inter-atomic potential, and it is the topic of discussion in the next section.

2.2 Quantum-Classical Molecular Dynamics

Several approaches pointing the way to a quantum-based MD have been proposed, starting in 1976 with the Quantum Mechanical/Molecular Mechanical (QM/MM) approach of Warshel and Levitt (Warshel and Levitt (1976)). The authors proposed breaking the Hamiltonian of the system into a reactive part; where quantum mechanics would be used (typically employing DFT), a non-reactive classical part where some non-reactive force-field can be used, and a boundary part that takes into account the Coulomb interactions between all electrons and MM partial charges (calculated by e.g. EEM), between all nuclei/ions and MM partial charges, and finally an analytic van der Waals interaction between the atoms. This QM/MM method

Table 2.4: List of partial charges calculated for a subset of small lithiated molecules, using GE to solve the EEM matrix.

Molecule	(Atom)	(EEM charge)	(DFT charge)
LiH	Li	0.2594	0.29
	H	-0.2594	-0.29
LiC	Li	0.2429	0.45
	C	-0.2429	-0.45
LiCH	Li	0.3070	0.41
	C	-0.2539	-0.55
	H	-0.0531	0.14
LiCH ₂	Li	0.4154	0.62
	C	-0.4275	-0.65
	H	-0.0060	0.02
LiCH ₃	Li	0.6609	0.37
	C	-0.6164	-0.81
	H ^{on(1)}	0.1002	0.22
	H ^{off(2)}	-0.0723	0.11

has been developed extensively and has found great application and popularity in molecular biology and biochemistry.

In 1985 another method was developed, by Car and Parrinello (CP) in (Car and Parrinello (1985)). The CP method extends the Kohn-Sham energy density functional by explicitly including the kinetic energy of all the nuclei and the overlap of the time differentiated orbitals. The required constraints are that the nuclear velocities are computed by taking the time-integral of the gradient (with respect to the nuclear coordinates) of the density functional and the 2nd time-derivative of a given orbital is proportional to the variation of the functional with respect to the conjugate orbital plus a Lagrange multiplier that ensures ortho-normality of the orbitals.

A more recent method based on a Tight-Binding (TB) approach to DFT was developed in the 1990s; it is similar in spirit to the CP method and is our method of choice to model the PMI using a quantum based method with reasonable scaling behavior. This Density Functional TB method (DFTB) is the subject of the next subsection.

2.2.1 Density-Functional Tight-Binding

The DFTB method is based on two theoretical approaches, DFT and TB. To give a historical outline, it is noted that in 1927 Thomas and Fermi ([Thomas \(1927\)](#); [Fermi \(1927\)](#)) proposed using the electron density to solve for electronic structure of the quantum many-body system. In the 1960s Hohenberg, Kohn, and Sham fully developed DFT ([Hohenberg and Kohn \(1964\)](#); [Kohn and Sham \(1965\)](#)) in its modern form. There are many reviews of Kohn-Sham-DFT (KS-DFT), see e.g. [Parr and Weitao \(1985\)](#), for further details on KS-DFT (DFT and KS-DFT are used interchangeably in the rest of the dissertation) we refer to [Hohenberg and Kohn \(1964\)](#); [Kohn and Sham \(1965\)](#); [Parr and Weitao \(1985\)](#) and references therein.

The Linear Combination of Atomic Orbitals (LCAO) approximation to Molecular Orbital (MO) theory was developed by Lennard-Jones, Pauling, Finklestein, and Horowitz; while for solids the LCAO method was developed by Bloch in his dissertation ([Bloch \(1928\)](#)). The TB approach was fully developed by Slater and Kostner in 1954 ([Slater and Koster \(1954\)](#)); it develops the LCAO specifically for band structure calculations in periodic systems by assuming that an Hamiltonian eigenstate of the system is equal to the sum of the Hamiltonian eigenstates of the isolated atoms and the Hamiltonian is replaced by a parameterized one whose elements depend on internuclear distance. In 1979, to meet this second requirement, Froyen and Harrison ([Froyen and Harrison \(1979\)](#)) proposed that the Hamiltonian matrix elements were related to internuclear distance by $1/r^2$. Also in 1979 Chadi ([Chadi \(1979\)](#)) suggested that the total energy of the system is given by:

$$E_{tot} = E_{band} + E_{rep}, \quad (2.30)$$

E_{band} is the sum of energies of all occupied orbitals (i.e. the band-structure) and E_{rep} is sum of repulsive terms between all atom pairs. In the 1990s Seifert et. al. ([Seifert et al. \(1996\)](#)) and Porezag et. al. ([Porezag et al. \(1995\)](#)) fully developed the DFTB method. Soon afterwards Elstner et. al. ([Elstner et al. \(1998\)](#)) extended

DFTB for the case of Self-Consistent Charging (SCC-DFTB). A brief derivation of the SCC-DFTB Hamiltonian is given below.

Yielding to arguments from Oliveira et. al. in (Oliveira et al. (2009)) one writes the electronic density as a reference density plus a small variation of the density, that is:

$$\rho(\vec{r}) = \rho_0(\vec{r}) + \delta\rho(\vec{r}). \quad (2.31)$$

Thus, the total KS-DFT energy is

$$\begin{aligned} E[\rho_0 + \delta\rho] = & \sum_i^M n_i \langle \Psi_i | -\frac{1}{2}\nabla^2 + v_{ext}(\vec{r}) + \int \frac{\rho'_0}{|\vec{r} - \vec{r}'|} d\vec{r}' + v_{xc}[\rho_0] | \Psi_i \rangle \\ & - \frac{1}{2} \iint \frac{\rho'_0(\rho_0 + \delta\rho)}{|\vec{r} - \vec{r}'|} d\vec{r} d\vec{r}' - \int v_{xc}[\rho_0](\rho_0 + \delta\rho) d\vec{r} \quad (2.32) \\ & + \frac{1}{2} \iint \frac{\delta\rho'_0(\rho_0 + \delta\rho)}{|\vec{r} - \vec{r}'|} d\vec{r} d\vec{r}' + E_{xc}[\rho_0 + \delta\rho] + E_{nn}. \end{aligned}$$

Noting that $\rho'_0 = \rho_0(\vec{r}')$ and $\delta\rho' = \delta\rho(\vec{r}')$, the first term after the matrix elements corrects for the double counting in the Coulomb term, the next term corrects for the XC contribution, the next term results from the Coulomb energy being split between ρ_0 and $\delta\rho$, and E_{nn} is the nuclear-nuclear repulsion. By taking a variation of E_{XC} with respect to the density, up to second-order, and noting that

$$\left(\frac{\delta E_{XC}}{\delta\rho} \right)_{\rho_0} = v_{XC}[\rho_0], \quad (2.33)$$

the energy of the system can be written as:

$$E = \sum_i^M n_i \langle \Psi_i | \hat{H}^0 | \Psi_i \rangle + E_{rep}[\rho_0] + E_{2nd}[\delta\rho, \rho_0]. \quad (2.34)$$

Here

$$\begin{aligned}
\hat{H}^0 &= -\frac{1}{2}\nabla^2 + v_{ext}(\vec{r}) + \int \frac{\rho'_0}{|\vec{r} - \vec{r}'|} d\vec{r}' + v_{xc}[\rho_0] \\
&= -\frac{1}{2}\nabla^2 + v_{KS}[\rho_0]
\end{aligned} \tag{2.35}$$

is a reference Hamiltonian, depending only on ρ_0 , and is analogous to E_{band} ,

$$E_{rep}[\rho_0] = -\frac{1}{2} \iint \frac{\delta\rho'_0\rho_0}{|\vec{r} - \vec{r}'|} d\vec{r}d\vec{r}' + E_{xc}[\rho_0] - \int v_{xc}[\rho_0]\rho_0 d\vec{r} + E_{nn} \tag{2.36}$$

defines the total repulsive potential, and finally the last term takes into account corrections to the energy arising from fluctuations in the density, given as:

$$E_{2nd} = \frac{1}{2} \iint \left[\frac{\delta\rho'_0\delta\rho}{|\vec{r} - \vec{r}'|} d\vec{r}d\vec{r}' + \left(\frac{\delta^2 E_{XC}}{\delta\rho'\delta\rho} \right)_{\rho_0} \right] d\vec{r}'d\vec{r}. \tag{2.37}$$

In non-SCC-DFTB E_{2nd} is neglected. By assuming the Born-Oppenheimer approximation and only considering valence orbitals, the Kohn-Sham equations are solved non-self-consistently (in that the output density need not be equal to the input density). The total energy of the system is taken as a sum of one and two-body potentials, given as:

$$E_0 = \sum_i^M n_i \langle \Psi_i | \hat{H}^0 | \Psi_i \rangle + E_{rep}. \tag{2.38}$$

To solve the KS equations the single particle wavefunctions are first expanded within a LCAO basis of Slater-type atomic orbitals ϕ_ν

$$\Psi_i(\vec{r}) = \sum_\nu^N C_{i\nu} \phi_\nu(\vec{r} - \vec{R}_\alpha). \tag{2.39}$$

These are found by solving a modified Schroedinger equation with a confining potential, given by:

$$\left(-\frac{1}{2}\nabla^2 + v_{KS}[\rho_0^\alpha] + \left(\frac{r}{r_0}\right)^2\right) \phi_\nu(\vec{r}) = \epsilon_\nu \phi_\nu(\vec{r}),^\dagger \quad (2.40)$$

with r_0 equal to twice the covalent radius of the free neutral atom. By applying the variational principle, we are led to the following set of equations:

$$\sum_{\nu}^N C_{i\nu} (H_{\mu\nu}^0 - \epsilon_i S_{\mu\nu}) = 0, \quad \forall \mu, i; \quad (2.41)$$

where

$$H_{\mu\nu}^0 = \langle \phi_\mu | \hat{H}_0 | \phi_\nu \rangle, \quad S_{\mu\nu} = \langle \phi_\mu | \phi_\nu \rangle, \quad \forall \mu \in \alpha, \nu \in \beta. \quad (2.42)$$

By the orthogonality condition we have:

$$H_{\mu\nu}^0 = \begin{cases} \epsilon_\mu^{freeatom} & \text{if } \mu = \nu \\ \langle \phi_\mu^\alpha | -\frac{1}{2}\nabla^2 + v_{KS}[\rho_0^\alpha + \rho_0^\beta] | \phi_\nu^\beta \rangle & \text{if } \alpha \neq \beta \\ 0 & \text{otherwise;} \end{cases} \quad (2.43)$$

where μ is an orbital that belongs to the α^{th} atom and ν belongs to the β^{th} atom. Once these Hamiltonian and overlap matrix elements have been computed on a lattice for a pair of atoms, splines are used to interpolate between points that are not explicitly tabulated.

The repulsive terms are found by taking the difference between the band energy and the total DFT energy, i.e.

$$E_{rep}(R_{\alpha\beta}) = (E_{DFT}(R_{\alpha\beta}) - E_{band}(R_{\alpha\beta}))_{ref.struct.} \quad (2.44)$$

They are then fitted to cubic splines.[‡] Hence, during an optimization or MD simulation, there is no recalculation of the matrix elements once E_{band} and E_{rep} are determined.

[†]This is different for parameters we have developed, as the Dirac-Kohn-Sham equations are solved, as will be discussed in the next subsection.

[‡]Quartic splines for the parameters we have developed, to be discussed in the next subsection.

In order to include the second-order density fluctuations to the energy, the total variation of the density ($\delta\rho$) is written as a superposition of atom-centered fluctuations which, under the monopole approximation, take the form of:

$$\delta\rho_\alpha \propto \Delta q_\alpha F_{00}^\alpha Y_{00} \quad (2.45)$$

Δq_α , is the difference between the population of electrons from a Mulliken population analysis [Mulliken \(1955\)](#) and the number of electrons in the free neutral atom. F_{00}^α is exponentially decaying radial function, and Y_{00} is the angular dependence (here we assume spherical symmetry). Hence, the second-order term becomes:

$$\begin{aligned} E_{2^{nd}} &= \frac{1}{2} \sum_{\alpha,\beta}^N \Delta q_\alpha \Delta q_\beta \iint \left[\frac{1}{|\vec{r} - \vec{r}'|} + \left(\frac{\delta^2 E_{XC}}{\delta\rho'\delta\rho} \right)_{\rho_0} \right] F_{00}^\alpha F_{00}^\beta Y_{00}^2 d\vec{r} d\vec{r}' \\ &= \frac{1}{2} \sum_{\alpha,\beta}^N \Delta q_\alpha \Delta q_\beta \gamma_{\alpha\beta} \end{aligned} \quad (2.46)$$

In the limiting case where $|R_\alpha - R_\beta| = |r - r'| \rightarrow \infty$ one can show [Oliveira et al. \(2009\)](#); [Elstner et al. \(1998\)](#) that under the Generalized-Gradient Approximation (GGA), the density goes to zero and $\gamma_{\alpha\beta} \rightarrow 1/|R_\alpha - R_\beta|$. Thus one is left with only the Coulomb interaction between atomic partial charges:

$$E_{2^{nd}} = \frac{1}{2} \sum_{\alpha\beta}^N \frac{\Delta q_\alpha \Delta q_\beta}{R_\alpha - R_\beta} \cdot \S \quad (2.47)$$

In the opposite limit where $|R_\alpha - R_\beta| = |r - r'| \rightarrow 0$, $\gamma_{\alpha\beta}$ describes the electron-electron interaction within the α^{th} atom and is related to the chemical hardness, or Hubbard parameter (U_α); i.e. $\gamma_{\alpha\alpha} = 2\eta_\alpha = U_\alpha$. By using Janak's theorem [Janak \(1978\)](#), the atom hardness is related to the change in the HOMO energy with respect to the occupation number like so:

[§]We note that this long range term for periodic systems is calculated with the Ewald summation.

$$\eta_\alpha = \left(\frac{\partial \epsilon}{\partial n} \right)_\alpha = \left(\frac{\partial^2 E[\rho_0]}{\partial n^2} \right)_\alpha \equiv \left(\frac{\partial^2 E[\rho_0]}{\partial q_\alpha^2} \right)_\alpha = \frac{1}{2} U_\alpha. \quad (2.48)$$

To remain consistent with the above mentioned assumptions, the reference density is assumed to be a Slater-type function that exponentially decays as:

$$\rho_\alpha(\vec{r}) = \frac{\tau_\alpha^3}{8\pi} e^{-\tau_\alpha |\vec{r} - \vec{R}_\alpha|} \quad (2.49)$$

Inserting this into equation 2.37, neglecting the contribution of E_{XC} , and integrating over r' one finds ,after some coordinate transformations (see [Oliveira et al. \(2009\)](#); [Eltner et al. \(1998\)](#)),

$$\gamma_{\alpha\beta} = \frac{1}{R} - s(\tau_\alpha, \tau_\beta, R), \quad (2.50)$$

where s is a short-ranged exponentially decaying function with the limit for $R \rightarrow 0$ of

$$s(\tau_\alpha, \tau_\beta, R) \rightarrow \frac{5}{16} \tau_\alpha + \frac{1}{R}. \quad (2.51)$$

Under the assumption that the Hubbard parameter well-approximates the second-order contribution to the energy, the exponent becomes

$$\tau_\alpha = \frac{16}{5} U_\alpha. \quad (2.52)$$

Therefore, we may now write our total SCC-DFTB energy that includes charge-density fluctuations in the following way:

$$E_{SCC}(R) = E_{band}(R) + E_{rep}(R) + \frac{1}{2} \sum_{\alpha,\beta}^N \gamma_{\alpha\beta} \Delta q_\alpha \Delta q_\beta. \quad (2.53)$$

Again $\Delta q_\alpha = q_\alpha - q_\alpha^0$, with q_α^0 being the number of electrons in the free neutral α^{th} atom, and q_α comes from a Mulliken population analysis:

$$q_\alpha = \frac{1}{2} \sum_i^M n_i \sum_{\mu \in \alpha}^N \sum_{\nu}^N (C_{i\mu} C_{i\nu} S_{\mu\nu} + C_{i\nu} C_{i\mu} S_{\nu\mu}) \quad (2.54)$$

Thus the Hamiltonian matrix elements between any two orbitals can be written as:

$$H_{\mu\nu} = H_{\mu\nu}^0 + \frac{1}{2} S_{\mu\nu} \sum_{\xi}^N (\gamma_{\alpha\xi} + \gamma_{\alpha\xi}) \Delta q_{\xi} = H_{\mu\nu}^0 + H_{\mu\nu}^1, \quad \forall \mu \in \alpha, \nu \in \beta. \quad (2.55)$$

Finally, by applying the Feynman-Hellman theorem ([Feynman \(1939\)](#)) the force on the α^{th} atom is given as:

$$\vec{F}_{\alpha} = - \sum_i^M n_i \sum_{\mu\nu}^N C_{i\mu} C_{i\nu} \left[\frac{\partial H_{\mu\nu}^0}{\partial R_{\alpha}} - \left(\epsilon_i - \frac{H_{\mu\nu}^1}{S_{\mu\nu}} \right) \frac{\partial S_{\mu\nu}^0}{\partial R_{\alpha}} \right] - \frac{\partial E_{rep}}{\partial R_{\alpha}} - \Delta q_{\alpha} \sum_{\xi}^N \frac{\partial \gamma_{\alpha\xi}}{\partial R_{\alpha}} \Delta q_{\xi} \quad (2.56)$$

This method is also extended to include dispersion/London forces by adding an additional potential of the following form:

$$U_{\alpha\beta}(R) = \begin{cases} d_{\alpha\beta} \left[-2 \left(\frac{\sigma_{\alpha\beta}}{R} \right)^6 + \left(\frac{\sigma_{\alpha\beta}}{R} \right)^{12} \right] & \forall R \geq \sigma_{\alpha\beta} \\ \frac{396}{25} d_{\alpha\beta} - 2^{5/6} \frac{672}{25} \frac{d_{\alpha\beta}}{\sigma_{\alpha\beta}^5} R^5 + 2^{2/3} \frac{552}{25} \frac{d_{\alpha\beta}}{\sigma_{\alpha\beta}^{10}} R^{10} & \forall R < \sigma_{\alpha\beta} \end{cases} \quad (2.57)$$

The form of this potential, i.e. the polynomial term, was chosen to avoid issues arising from the short-range London repulsion between adjacent atoms see [Oliveira et al. \(2009\)](#). Thus to the (SCC)DFTB energy is also added

$$E_{disp} = \frac{1}{2} \sum_{\alpha, \beta}^N U_{\alpha\beta}(R). \quad (2.58)$$

For further details on DFTB, see [Porezag et al. \(1995\)](#); [Elstner et al. \(1998\)](#); [Oliveira et al. \(2009\)](#). In the next subsection we go into some detail on the methods

employed for the, so-called, Slater-Kostner parameter files we have developed for use in SCC-DFTB.

2.2.2 Development of DFTB Parameters

We have used a method originally developed by Desclaux (Desclaux (1970, 1975)) and further improved on by Witek et al. (Witek et al. (2007)), to find Eigenfunctions of the Dirac-Kohn-Sham (DKS) equations. This method is an all-electron calculation, solved numerically on a fine mesh, to determine the atomic orbitals used to compute the Hamiltonian and overlap matrix elements. Use of the DKS equation is physically motivated in order to treat all atoms across the periodic table on equal footing. In particular we have developed parameters not only involving light elements (H, He, Li, Be, C, O) but also for the heavy metals (Mo and W). The DKS equation is given by:

$$[-i c \alpha \nabla + (\beta - \mathbf{1} + \mathbf{v}_{\text{eff}})] = \epsilon_j \phi_j \quad (2.59)$$

Here, α and β are the Dirac matrices and ϵ_j is the energy of the j^{th} 4-component spinor ϕ_j , and c is the speed of light. The effective potential is given by:

$$v_{\text{eff}} = v_{\text{nuc}} + v_{\text{Coul}} + v_{\text{XC}} + v_{\text{conf}}, \quad (2.60)$$

where v_{nuc} is the attractive nuclear potential, v_{Coul} is the Coulomb repulsion between quasi-electrons/positrons, v_{XC} is the exchange-correlation potential (given by the PBE functional in this case), and v_{conf} is the confining potential. Motivated by the requirements that the potential be negligible near the atomic core and quickly increase outside of the region of the atomic radius, and to ensure that it transforms as a time-like component of a Lorentz 4-vector (as the other terms in the Hamiltonian do), the Wood-Saxon potential Woods and Saxon (1954) is used:

$$v_{conf} = \frac{W}{1 + e^{-a(r-r_0)}}. \quad (2.61)$$

Here the well-depth W , the slope of the potential a , and the potential's "width" r_0 are parameters that can be optimized. Optimized parameters were already determined by the Henryk Witek's group at the National Chiao-Tung University in Taiwan for all elements except Mo and W; which we fitted to reproduce band-structure data from Projector Augmented Wave-DFT, PAW-DFT(PBE).

The four-component Dirac spinor is

$$\phi_j = \frac{1}{r} \begin{pmatrix} P_j(r)\chi_\kappa^m \\ iQ_j(r)\chi_{-\kappa}^m \end{pmatrix} \quad (2.62)$$

χ 's are two-component spinors obtained by multiplying appropriate spherical harmonics by the spin eigenfunctions. By assuming spherical symmetry and then by averaging over the spin-orbit split components of p, d, and f orbitals we may write the radial components of the Dirac spinor as:

$$\begin{pmatrix} P_l(r) \\ Q_l(r) \end{pmatrix} = \frac{l}{2l+1} \begin{pmatrix} P_{\kappa=l}(r) \\ Q_{\kappa=l}(r) \end{pmatrix} + \frac{l+1}{2l+1} \begin{pmatrix} P_{\kappa=-l-1}(r) \\ Q_{\kappa=-l-1}(r) \end{pmatrix} \quad (2.63)$$

where P and Q are the radial parts of the upper and lower 2-component spinors, κ is the relativistic spinorial angular quantum number ($\kappa = l(l+1) - (j+1/2)^2$, where j is the total angular momentum), and l is the scalar-relativistic angular momentum quantum number.[¶] We note that $Q \propto P/c$ and hence will be small, therefore it is neglected; thus the wavefunctions for DFTB are given by:

$$\Psi_{nlm} = P_{nl}(r)Y_{lm}. \quad (2.64)$$

The Y_{lm} are the spherical harmonics and P_{nl} is the Slater-type orbital that depends on the Wood-Saxon parameters:

[¶]The effects of spin-orbit coupling are not included in this approach.

$$P_{nl}(r) = b \exp \left[- \left(\sqrt{-2(\epsilon - W) - \frac{(\epsilon - W)^2}{c^2}} \right) r \right]. \quad (2.65)$$

Here b is simply an adjustable constant. The spinorial orbital energies are related to the scalar-relativistic ones by the following formula:

$$\epsilon_l = \frac{l}{2l+1} \epsilon_{\kappa=l} + \frac{l+1}{2l+1} \epsilon_{\kappa=-l-1}. \quad (2.66)$$

The Hamiltonian and overlap matrix elements, and the Hubbard parameters, are calculated as before; relativistic effects are taken into account by the compression of s and p orbitals and the stretching of d orbitals. Since the Hamiltonians and overlaps of interest involve combinations of s , p , and d orbitals; we are interested in the following bonds^{||}

$$\sigma_{dd}, \pi_{dd}, \delta_{dd}, \sigma_{pd}, \pi_{pd}, \sigma_{pp}, \pi_{pp}, \sigma_{sd}, \sigma_{sp}, \quad \text{and} \quad \sigma_{ss}$$

Therefore, there are twenty integrals (ten Hamiltonians and ten overlaps) to calculate. These integrals are computed from 0.0 to 5.5 Å in increments of ≈ 0.01 Å. From these the band-structure energy (i.e. the attractive part of an interatomic potential) was found using DFTB. Again using DFT data to find the total energy as a function of distance of reference systems (small molecules for systems with H and C and solid-state calculations by varying the lattice constant in W(bcc) for example), repulsive pair terms were found and fit to quartic splines. For atom-pairs involving helium the Ziegler, Biersack, and Littmark (ZBL) potential was used in place of the total DFT energy and repulsive potentials were computed from these. Likewise, in order to model very short-distance (≤ 1 Å) behavior ZBL data was used to determine the repulsive splines between all atom pairs. Finally, at distances between 0 and about 0.01 Å the ZBL potential was fit to a decay equation of the following form:

^{||}We note that during the integration, the direction of r_0 is chosen so that the appropriate orbitals have the correct orientation for σ , π , and δ bonding.

$$e^{-a_1 r + a_2} + a_3 \tag{2.67}$$

We have helped develop the Slater-Kostner parameter files, i.e. the Hamiltonian and overlap integrals and the repulsive splines used by DFTB, for two families of materials, H-He-C-O-Li-Mo and H-He-C-Be-W. For further details of this method please see (Desclaux (1970, 1975); Witek et al. (2007)) and references therein. These Slater-Kostner parameters will enable future research of the PMI, and may have application in various branches of materials science.

We note that all simulations in the next chapter use parameters that were developed by Bremen (2010) and for pairs involving Li by Morokuma (2010). These parameters do not use the all-electron DKS equations to determine the Slater-type orbitals. Instead, as explained above, a modified Schroedinger equation is solved with the v_{KS} potential (using B3LYP), and the harmonic confining potential.

In the next chapter we present our results of physical-chemical processes at the PMI, using the aforementioned original classical potentials for hydrocarbons, as well as the improved ones, and the quantum-based potentials for Li-C-O-H, for surfaces of amorphous carbon (mixed with other materials), bombarded by isotopes of hydrogen.

Chapter 3

Physical-Chemical Processes at the Plasma-Material Interface

Plasma particles will have energies up to a few keV. Surface modification will arise from physical and chemical sputtering leading to erosion and particle retention; combined with morphological changes such as displacements, vacancies, and blistering. Chemically or physically sputtered particles, for example hydrocarbons (like methane or acetylene) or tungsten, will pollute the plasma resulting in energy loss, thus degrading reactor performance. Tritium may become trapped in plasma-facing surfaces and tritiated molecules can be re-deposited on surfaces raising the issue of containing radioactive waste for time-scales of about 100 years. It is of critical importance to quantify reaction rates of these processes to minimize these effects.

Figure 3.1 shows some examples of simulation cells which are used to model interactions at the Plasma Material Interface (PMI). We note that the simulation cells for CMD simulations are about $(2.5 \text{ nm})^3$ containing a few thousand atoms; while the simulation cells for DFTB are about $(1.4 \text{ nm})^3$ containing a few hundred atoms. Periodic boundary conditions are always enforced in the plane of the interface (the $x - y$ plane). Again, in CMD simulations atoms are thermostatted with a Langevin thermostat; in DFTB a Nose-Hoover thermostat is used. To generate statistics for

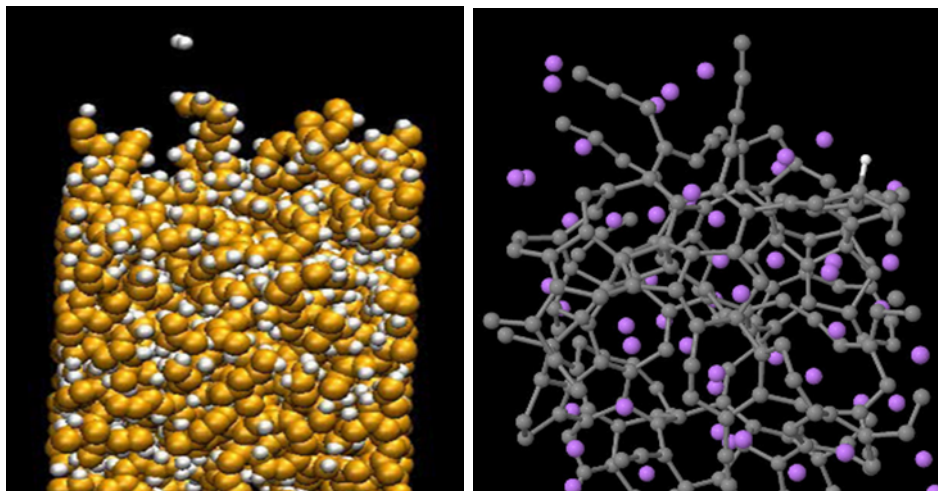


Figure 3.1: Renderings of a-C:D surface bombarded by D_2 (C in yellow, H in white) and a-C:Li with D retained (C in black, Li in purple, H in white)

sputtering simulations nearly 5000 independent random impact trajectories are used for each impact particle energy, type, etc.; employing an “embarrassingly parallel” Monte Carlo computational approach. In this chapter a few key chemical and physical reactions taking place at the PMI are explored. Follow-up future work is noted.

3.1 Energy and Temperature dependence of Chemical sputtering of a-C:D surfaces bombarded by D

The chemical sputtering of deuterated amorphous carbon (a-C:D) surfaces irradiated by 1-50 eV deuterium atoms at surface temperatures between 300 and 1000 K was studied using CMD, [Dadras and Krstic \(2011\)](#). A quasi-stationary state was reached by cumulative bombardment for each energy and temperature. When compared with experiment, the results did not show a temperature dependent peak in the sputtering yields that has been observed in beam-surface experiments of [Mech et al. \(1998\)](#); [Balden and Roth \(2000\)](#). It was hypothesized that the reason for this disagreement between experiment and simulation lies in the incapability to model thermally induced

processes of diffusion and desorption, which evolve at time scales beyond those that can be described by CMD. A successful attempt was made to correct this absence of the thermally stimulated desorption/degassing of hydrogen from the MD simulations.

While the surfaces of the near-future pulsed (400s) experimental fusion machine (ITER) are kept cold, close to room temperature, the temperatures of the plasma-exposed surfaces in reactors that would be capable of energy conversion (DEMO) have to be elevated, possibly to ≈ 1000 K (Marmar et al. (2009); Wong (2009); Andreani et al. (2006); Norajitra et al. (2008)). This motivates our study of the sputtering yield as function of surface temperature, for surfaces bombarded by hydrogen particles in the least studied chemical sputtering energy range (i.e. below 50 eV).

There are few theoretical/simulation studies of sputtering yields in this energy region; Salonen et. al. (Salonen et al. (2001)) obtained results for a virgin (i.e. not cumulatively bombarded) a-C:T surface (tritiated to T/C = 0.4) irradiated by a tritium atoms following a Maxwell-Boltzmann distribution of impact energies with $E_{rms} = 10$ eV, and for a range of incident angles. The authors of Salonen et al. (2001) found a noticeable peak in the sputtering yield around 900 K, claiming that this peak persists also for other surfaces composed of different hydrogen isotopes. We were unable to reproduce their results with a “virgin” surface at the single impact energy of 10 eV (see figure 3.2).

The temperature dependence of the chemical sputtering yield of graphite bombarded by D has been studied experimentally by Mech et. al. (Mech et al. (1998)) and Balden et. al. (Balden and Roth (2000)). The authors of Mech et al. (1998) used a beam of D^{2+} and employed a quadrupole mass spectrometer to find the yield of carbon atoms, Y_{chem} , from the yield of a collection of ejected stable hydrocarbons $Y_{chem} = ((CD_4 + 2(C_2D_2 + C_2D_4 + C_2D_6) + 3(C_3D_6 + C_3D_8))/D$. In Balden and Roth (2000) a beam of D^{3+} ions was used, and the total chemical erosion was determined from weight loss measurements. As can be seen in figure 3.3, the results of Balden and Roth (2000) are about five times larger than those of Mech et al. (1998). Both the difference in impacting molecular ions and of the method of erosion

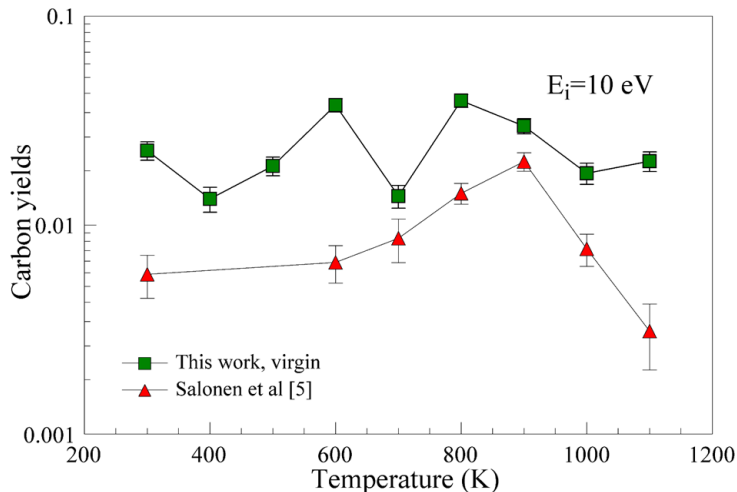


Figure 3.2: Comparison of carbon sputtering yields from simulations of [Salonen et al. \(2001\)](#) for plasma bombarding an a-C:T surface (triangles) with results of this work for a virgin a-C:D surface bombarded by 10 eV deuterium (squares). Error bars of the current results show the standard error obtained from one surface, the data from [Salonen et al. \(2001\)](#) show the standard error from 6 different surfaces. Figure from [Dadras and Krstic \(2011\)](#).

measurements could cause a discrepancy in these results (see [Meyer et al. \(2011\)](#)). The measurements show a noticeable peak in the sputtering yield at around 600 - 700 K. We note that our calculation of the total carbon erosion yields in figure 3.3 include all ejected hydrocarbons C_xD_y which satisfy $x \leq 4$, and are in a better agreement with measurements of [Balden and Roth \(2000\)](#). Further details on the various experimental and theoretical aspects of the chemical sputtering, including its dependence on the surface temperature can be found in [Jacob and Roth \(2007\)](#) and references therein.

In other works ([Krstic et al. \(2007b\)](#); [Stuart et al. \(2007\)](#); [Krstic et al. \(2007a, 2009\)](#); [Reinhold et al. \(2009\)](#)) the authors demonstrated that CMD simulations using the Brenner-Tersoff Reactive Empirical Bond-Order (REBO) potential of [Brenner et al. \(2002\)](#) could produce results in agreement with experimental data on specific hydrocarbons (methane, acetylene) chemical sputtering yields for a range of incident atom energies for surfaces at room temperature. The key element of that success was mimicking as much as possible the conditions in beam-surface experiments. This

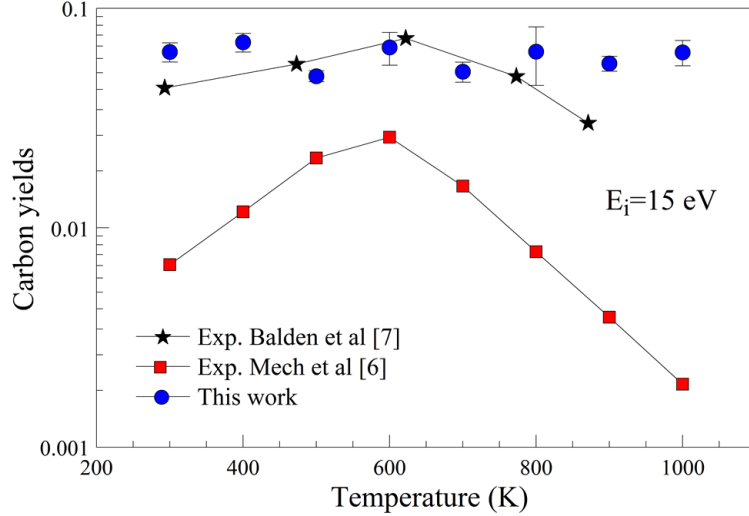


Figure 3.3: Comparison of sputtering yields for surfaces bombarded by 15 eV deuterium as a function of surface temperature. Experimental data of [Mech et al. \(1998\)](#) (hollow squares) and [Balden and Roth \(2000\)](#) (stars); [Dadras and Krstic \(2011\)](#) (filled circles) with error bars representing standard error obtained from 6 different surfaces.

was achieved by cumulatively bombarding the surface until a quasi-steady-state was reached, defined by the total hydrogen yield $Y_H \approx 1 \pm 0.2$ per impact hydrogen atom; ejected in the form of either hydrogen atoms, molecules, or hydrocarbons. Such surface preparations were done separately for each impact energy and type of particle, requiring a number of impacting particles, typically in the range of 1000-2000 impacts per case. The particle-surface simulations at a given impact energy were then performed on a number of surfaces with various cumulated fluences, with thousands of impact trajectories until satisfactory statistical weights of the desired results were achieved. In the present study the same approach was applied, extending it over a range of surface temperatures T (300 to 1000 K).

The surface is modeled by a cell of amorphous deuterated carbon (a-C:D) with dimensions of approximately $(2.5 \text{ nm})^3$ and of about 2,500 atoms. The initial, “virgin,” cell was created by succession of heating (to 10^4 K) and annealing (to 300 K) a carbon bulk (randomly deuterated to about 40% of D/C). Such a “virgin” cell was cut into a cube, 2D periodic boundary conditions applied, and was then heated

to a desired temperature by a Langevin thermostat, and relaxed for 100 ps. Keeping the surface thermostatted at a chosen T , the surface was cumulatively bombarded by deuterium atoms at various energies, in the range $E_i = 1 - 50$ eV. For each T and E_i , six surfaces which underwent between 1000 - 2000 impacts (where they reached the quasi-steady state) were selected for sputtering simulations. The motion of atoms in the bottom 2 Å of the simulation cell was frozen in the direction of impact (Z), to prevent motion of the whole cell. Finally, each of the chosen cumulatively bombarded surfaces was relaxed for 100 ps.

In our study (Dadras and Krstic (2011)), a surface prepared by cumulative bombardment (and heated to given temperature), is used for the sputtering simulations by a D atom of appropriate energy, impacting normally to the surface, at a random location in the plane (X, Y) of the simulation cell interface. The simulation is allowed to run for at least 30 ps, to collect all sputtered particles. The surface is then reset and this process is repeated for 4800 random impact trajectories. Total number of trajectories used in this work, for all considered impact energies and surface temperatures exceeds seven million. Sputtering yields are calculated and averaged over all trajectories, followed by averaging over the six different surfaces at a given T and E_i . The reported error bars in most cases reflect the standard error of dispersion of the results across these six surfaces. It is noted that the results from the surfaces which turned out not to be in the steady state (total hydrogen yield differed from unity by more than 20%) are not taken into account. Our total sputtering yield, reported in this work is a sum over all hydrocarbon C_xD_y (and carbon, C_x) sputtering yields for $n \leq 4$, supported by most of the experiments on the chemical sputtering of carbon. As shown by Krstic et al. (2007b); Stuart et al. (2007); Krstic et al. (2007a, 2009); Reinhold et al. (2009), MD simulations using the REBO potential seem to significantly overestimate contributions of heavier hydrocarbons.

Our results for the total carbon sputtering are fairly constant across the considered temperature range, while available experiments in this impact energy and temperature range show a slow increase of the yield, peaking in range of 600-700 K, followed by

a steeper decrease with increasing temperature. A typical case is shown in figure 3.3, for the impact of 15 eV D. Although the calculated data agree in magnitude with the measurements of [Balden and Roth \(2000\)](#) within the margin of 50%, even oscillating around the experimental data, the trend of increase toward the 600-700 K peak is missing. We have observed in simulations a mild increase of the threefold-coordinated and the adequate drop of the fourfold-coordinated carbon with increase of temperature, but this was not enough to significantly influence the sputtering chemistry. Thus, it was hypothesized that increase of the carbon sputtering yield toward the peak value in the experiments could be assigned to the thermally increased diffusion of volatile molecules and atoms. Namely, the chemistry of the sputtering mainly happens at the end of the collision cascade of the impact atom, when it is almost thermalized. The higher impact energy means a deeper penetration, resulting in higher sensitivity to the diffusion rate and therefore the stronger dependence on the surface temperature, as confirmed in the temperature/energy dependences of measurements of the methane sputtering ([Jacob and Roth \(2007\)](#)). The drop of the available experimental yields with temperature (above 800K) we attribute to the intensive thermally induced diffusion and desorption of hydrogen from the surface. However, the thermal processes evolve at time scales much longer than ps considered by molecular dynamics, which is a possible explanation for absence of a clear peak in our results, as well as absence of a more essential drop at high temperatures. It was postulated that the hydrogen content of the surface is the precursor for chemical sputtering, and it is illustrated at the end of this section by a numerical experiment that the loss of hydrogen can be a cause for the reduced sputtering at higher temperatures.

A 3D plot of the carbon sputtering yields as a function of both surface temperature and impact energy is presented in figure 3.4, and compared with available experimental data of [Balden and Roth \(2000\)](#). This figure illustrates comprehensively the general trends of both measured and simulated data in the considered ranges of impact energy and surface temperatures. The calculated data stay acceptably close

(within 50%) to the measured yields at temperatures below 700K, though without showing a particular trend. At temperatures above about 800 K (as was also the case in Figure 3.4) our results do not follow the trend of the measured data to decrease with temperature. However, a drop is seen in the case of 50 eV, which we consider an exception to the rule possibly caused by the fact that 50 eV is the border line of applicability of the REBO potential. As discussed above, we hypothesized that the reason for the measured drop in the sputtering yield at higher temperatures is thermally stimulated diffusion and desorption of hydrogen from the surface. We note that recent experimental results of Doerner et. al. (Doerner et al. (2009)) show a strong release of D from carbon upon heating, a process that starts already at 500 K. At 1 eV impact our simulations produce total carbon yields below 10^{-3} , in agreement with previous modeling of Krstic et al. (2009), as well as with modeling of Salonen et al. (2001), reflecting his “swift chemical sputtering” mechanism (see Jacob and Roth (2007)). Chemical erosion of amorphous carbon induced by thermal hydrogen atoms, which can reach significant yields (see Jacob and Roth (2007)), evolves at much longer time scales not reachable by MD.

In order to speed up the deuterium desorption the hydrogen was “over-heated” in the simulation cell to 5000 K (while keeping the carbon frozen, to prevent the cell “exploding”). The surface was relaxed and thermostatted for 100 ps to its original temperature, and then the sputtering simulations were repeated with such a prepared surface. This process was repeated for various lengths of time of over-heating until agreement with experiments of Balden and Roth (2000) was reached. Figure 3.5(a-c) shows the results for the sputtering yields by employing the above method for 15 eV, 20 eV, and 30 eV impact energies; which illustrates well the hypothesized reason for the drop of measured sputtering yields. Using the same surfaces, predictions are made of the methane and acetylene sputtering yields in figure 3.5 (d-f), which give the “corrected” values in the range 800-1000 K. We note that emission of methane is strongly dependent on the sp^3 hybridization content in the surface (Krstic et al.

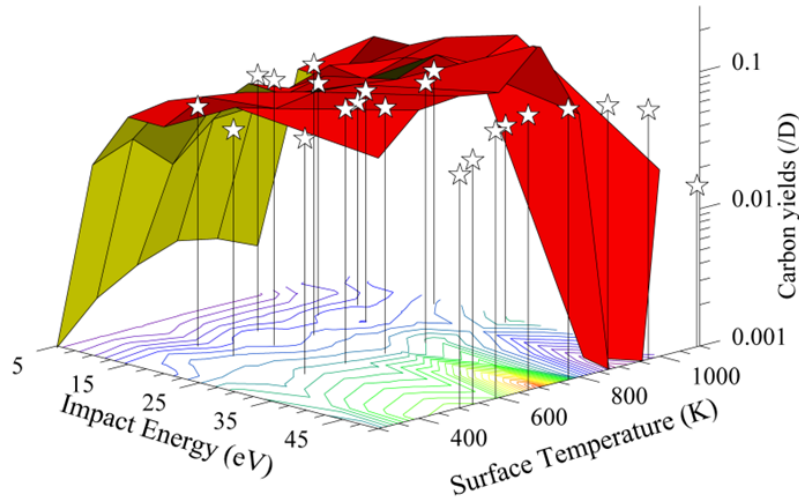


Figure 3.4: 3D plot of the carbon sputtering yield as a function of both surface temperature and energy of the impacting particle, compared to experimental data from Balden and Roth (2000) (hollow stars); figure from Dadras and Krstic (2011)

(2007b)), which is not warranted by our method of stimulated release of hydrogen, and that these predictions should be accepted with caution.

Finally, the needed reductions of the hydrogen content are shown in figure 3.6, running between 5% and 30% for D/D_0 , where D is the amount of deuterium atoms in the simulation cell after over-heating and D_0 is the number of deuterium atoms before over-heating (i.e. immediately after being cumulatively bombarded). To explain the deviation of the point at 900 K for $E_i = 30$ eV from the trends of 15 and 20 eV we note in figure 3.2c that, unlike the cases for 15 and 20 eV, the original (not-corrected) sputtering yield for 900 K is noticeably below those at 800 and 1000 K. The “right” contents of D at temperatures between 800-1000 K for fitting the total carbon yields with experimental values in Balden and Roth (2000) were found after trying over-heating for various durations of time, resulting in various D/D_0 and various sputtering rates until the agreement with measurements was reached. It is also interesting to compare the rate of the thermally induced decrease of the deuterium content in carbon obtained by this “trial-and-error” method and those obtained in Doerner et al. (2009)

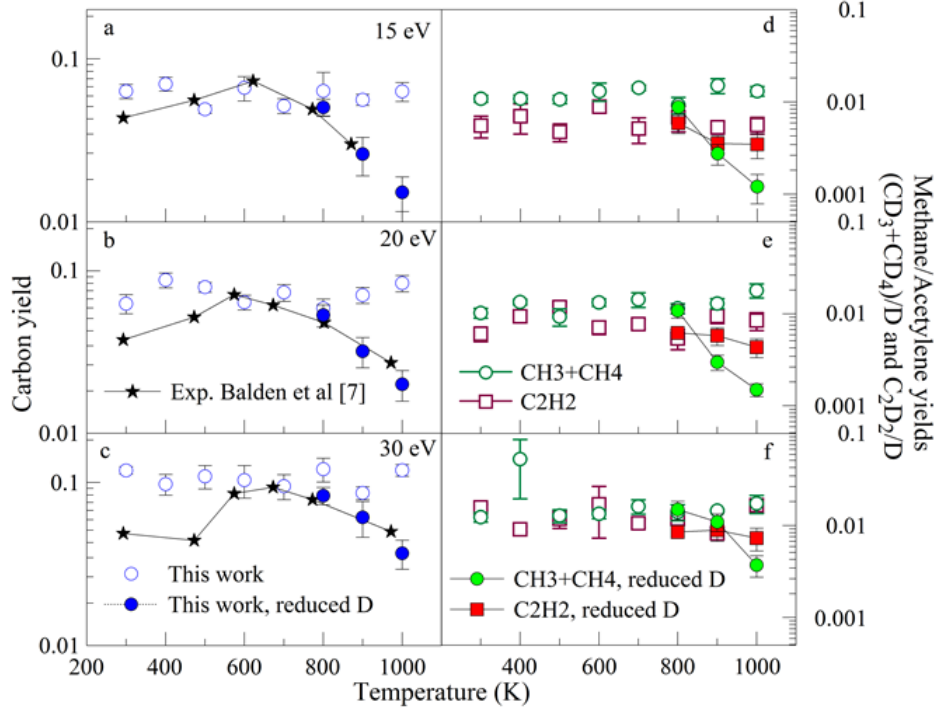


Figure 3.5: Total carbon sputtering yields before (hollow circles) and after (filled circles) "super-heating," compared to experiments (filled stars) of [Balden and Roth \(2000\)](#); for various impact energies (a - c). Methane and acetylene sputtering yields before (hollow symbols) and after (filled symbols) super-heating, for various energies (d - f). Figure from [Dadras and Krstic \(2011\)](#).

by fitting to the measured D content. The slope of D/C (or D/D₀ here, since C content was kept constant during the over-heating) from [Doerner et al. \(2009\)](#) is proportional to $e^{2268/T}$, presented in figure 3.6.

The fact that the present calculations disagree with those of [Salonen et al. \(2001\)](#) deserves additional discussion. In ([Salonen et al. \(2001\)](#)), the authors discuss that the cells were heated slowly to the given temperature, and that during the heating the fraction of three and four-fold coordinated carbon sites in the cell increased with increasing temperature. In the present case, the simulation cell was thermostatted for 100ps (which is slow) with a Langevin thermostat with time constant of 100 fs, then relaxed (free evolution) for 100 ps. Figure 3.7 shows the change of the moiety fraction in the whole cell between final (i.e. the over-heated and relaxed surfaces at various temperatures) and initial "virgin" surfaces (which was not over-heated).

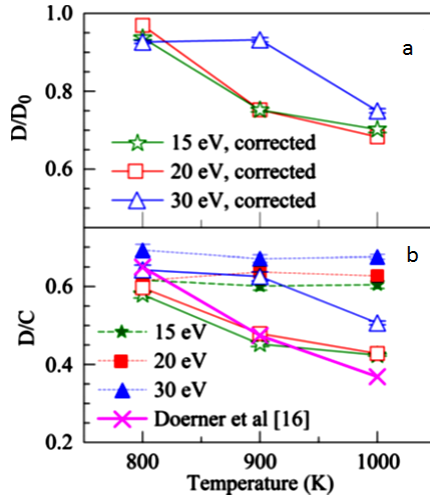


Figure 3.6: Reduction of deuterium from super-heating. Shown are fraction a) D/D_0 at various impact energies and b) D/C , after and prior to forced deuterium release. Measurements of the thermally induced release rate from Doerner et al. (2009) is shown by X symbols. Figure from Dadras and Krstic (2011).

As is shown here also the fraction of threefold coordinated carbon increased, while the fourfold coordinated decreased, like with Salonen et al. (2001), but this was not enough to explain the T-dependence as obtained by Salonen et al. (2001) with the “virgin” surface. Figure 3.8 shows the change of three-fold and four-fold moieties as functions of T for the cumulated (steady-state) cases. The change of moieties is even more pronounced than in the virgin case, but do not result in a peak of the sputtering yields with temperature.

Classical molecular dynamic simulations were used to model chemical sputtering from a-C:D surfaces, prepared at various surface temperatures in the range of 300-1000 K, bombarded by deuterium atoms for a range of impact energies, 1-50 eV. Our results do not show a temperature dependent peak in the sputtering yields that has been observed in beam-surface experiments (Mech et al. (1998); Balden and Roth (2000); Meyer et al. (2011)). We hypothesize that the reason for this disagreement between experiment and simulation lies in the incapability to model thermally induced stimulated processes of diffusion and desorption, which evolve at time scales beyond

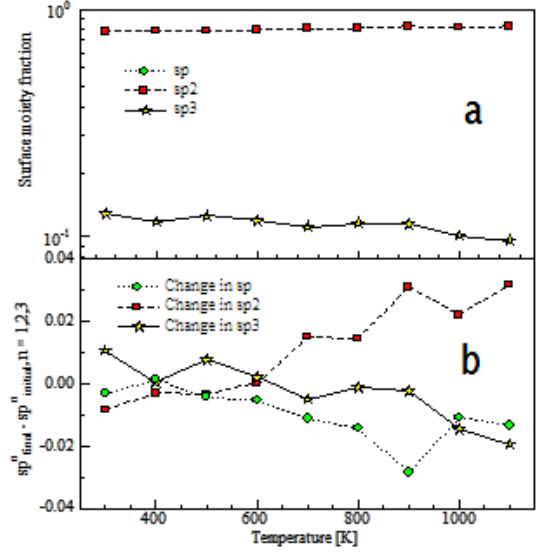


Figure 3.7: Moiety fraction in the whole cell between final, i.e. over-heated, (b) and initial “virgin” (a) surfaces.

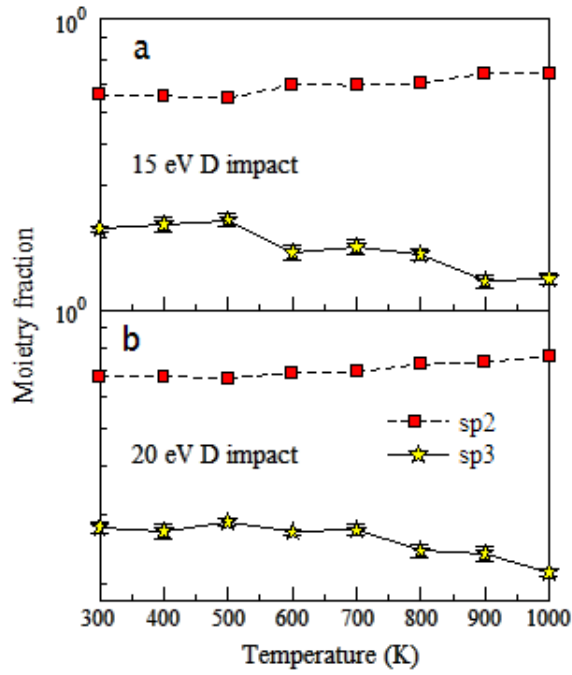


Figure 3.8: Change of 3-fold and 4-fold moieties as functions of T for the cumulatively bombarded surfaces, for 15 (a) and 20 eV (b) impact energy. The change of moieties is even more pronounced than in the “virgin” case, but do not result in a peak of the sputtering yields with temperature.

those that can be described by MD (which is only applicable for a range between ps and ns). By over-heating the simulation cell we forced partial release of deuterium from the cell, and successfully found, by trial-and-error, the deuterium release fractions by fitting carbon sputtering yields to experimental data of [Balden and Roth \(2000\)](#).

3.2 Sputtering Results from Refitted-REBO

Using the RREBO (discussed in the previous chapter), sputtering simulations were also carried out in [Kent et al. \(2011\)](#); the methane, acetylene, and total carbon yields as a function of impact energy are shown in Figure 3.9 (a - c). Interestingly, the results with REBO and RREBO potentials do not show a drastic difference in the sputtering yields. However, RREBO shows somewhat improved comparison with experimental values. It is noted that earlier results (e.g. [Krstic et al. \(2007b\)](#)) found that yields of $CD_3 + CD_4$ from simulations agree with methane yields from beam-surface experiments. To test if this difference came from a possibly incomplete definition of methane in REBO, it was re-parameterized in RREBO, with special attention to its accurate representation. This did not influence the discrepancy between theory and experiments of [Meyer et al. \(2011\)](#) in CD_4 indicating that the problem has not been resolved. Figure 3.9b shows sputtering yields of acetylene obtained by REBO and RREBO potentials, compared with measured C_2D_y yields from an ATJ graphite target by [Meyer et al. \(2011\)](#). While the REBO results show a sharp increase of the yields above 30 eV impact energy, RREBO yields have this trend significantly reduced, approaching the experimental values. Finally, summing the yields of all hydrocarbons C_xD_y for $x \leq 4$ and comparing these with the measured summed yields of the ejected hydrocarbons from [Meyer et al. \(2011\)](#) (figure 3.9c), the simulation yields stay above the measured yields by about a factor two. The new RREBO potential, similarly to REBO, was not able to resolve this increase in the total modeled-to-measured carbon yields.

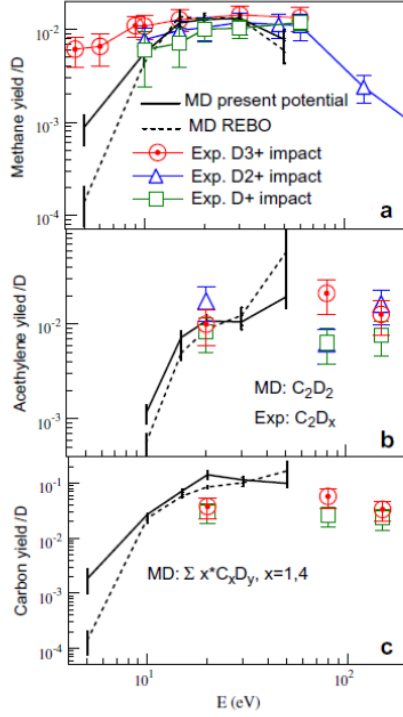


Figure 3.9: Sputtering yields obtained by bombardment of a-C:D by D at various impact energies: a) $CD_3 + CD_4$ of CMD and experimental results on CD_4 . b) C_2D_2 of CMD with C_2D_y of experiments. c) total carbon yield C_xD_y for $x \leq 4$ and CD_x , C_2D_2 , C_2D_4 , C_2D_6 , C_3D_6 and C_3D_8 from experiments of Meyer et al. (2011), figure from Kent et al. (2011).

3.3 Dynamics and Chemistry of Surfaces of Lithiated and Oxygenated Carbon, Bombarded by Deuterium

This section is based on two publications Krstic et al. (2011); Dadras et al. (2012). The use of lithium as a plasma-facing surface in magnetic confinement fusion devices is increasingly becoming popular. Mostly due to its impurity gettering and ability to retain hydrogen (low recycling regimes). National Spherical Torus Experiment (NSTX) Bell et al. (2009) uses lithium deposition on graphite substrates to enable important plasma control. One peculiar mystery in the past few years of lithiation efforts in NSTX is how ultra-thin films of lithium can affect the tokamak plasma

knowing that Li readily intercalates (diffuses) into the graphite bulk. The mechanism of hydrogen (deuterium is used in NSTX) bonding with lithiated graphite is not well understood and this research sought to elucidate this puzzle. Laboratory experiments by Taylor et. al. [Taylor et al. \(2011\)](#) have demonstrated a complex rich surface chemistry at play and with XPS analyses found that the presence of lithium has significant effects on the fundamental interactions of hydrogen with C and O atoms on ATJ graphite surfaces.

The main goal of the present research is to explain the specifics of the chemistry of deuterium bonding to lithiated carbon. In order to gain an understanding of the intriguing chemistry in a C-Li-O-H system we develop a computational approach for its simulation and validate it by experimental findings. As discussed in chapter 2, the main difficulty in the theoretical approach to this system is the low electronegativity of lithium. Thus, lithium has an electronegativity of 0.95 (Pauling), in comparisons to H (2.2), C (2.4) and O (3.4). In effect, in binding it will easily become electropositive, oxygen electronegative while H and C will find their place somewhere in between. In a “pure” hydrocarbon environment C and H will stay close to being electro-neutral. Long-range interactions when performing molecular dynamic simulations have been avoided in the past because of the possible prohibitive computational cost. Namely, it is difficult to study the Li dynamics theoretically because of its polarizing features when interacting with other elements. In consequence of partial charge transfer from Li to other atoms, the dominant long-distance binding force is the Coulomb attraction between opposite charges; i.e. bonding between Li and other atoms is mixed covalent and polar. The differences in electronegativity between constituent atoms in LiC, LiO and LiH systems are very large and therefore these systems could be considered as ionic solids.

The partial charges of the atoms that take part in these polar interactions depend on coordinates of all atoms in the system, and change typically in each simulation step, requiring a need for accurate calculation of the charge dynamics during the system evolution. Semi-empirical methods like the Electronegativity Equalization

Method (EEM) besides being of questionable accuracy might put a significant time lag on calculations with classical molecular dynamics. We chose a quantum-classical molecular dynamics approach, treating nuclei of the system as classical particles but performing adiabatic quantum-mechanical calculations of the electronic motion at each time step. We employ the SCC-DFTB method of [Eltner et al. \(1998\)](#) (discussed in detail in section 2.2), adapted for the trajectory Monte Carlo calculations in a multi-processor super-computer environment ([Krstic et al. \(2007b\)](#); [Jakowski \(2011\)](#)). This is an approximation to DFT, in which only valence orbitals are considered and difficult density integrals are parameterized and fitted in advance. In comparison to other tight-binding methods, this one has self-consistent calculation of atomic charges. The method still scales as N^3 (due to diagonalization step), but the corresponding size of basis set (Slater orbitals) is much smaller (up to 10 times) than in first principles DFT. Thus the method is significantly faster, up to a thousand times than first principles DFT, but is also slower than the CMD, falling into the range of current computational capabilities. Parameterization of the pair-parameters for the Li-C-O-H system is provided by the K. Morokuma and S. Maeda [Morokuma \(2010\)](#).

It is known from in-situ experiments at the Purdue lab, and in seven different tokamak machines (TFTR, CDX-U, FTU, DIII-D, TJ-II, EAST, and NSTX) that graphite with thin lithium coatings have a “significant” affect on plasma behavior and more specifically on hydrogen recycling. Controlled experiments demonstrated reduced recycling, improved energy confinement time, and a reduction of edge instabilities, i.e. suppression of Edge Localized Modes (ELMs)

The initial experimentalists conjecture was that there was some “functionality” that governed the behavior of the Li-C-O-H system observed indirectly by analyzing the O(1s) and C(1s) peaks, using XPS diagnostics. However, for a reason that was not clear at the time the Li(1s) peaks did not carry much information on the underlying chemistry, these were “invariant” to the changing experimental conditions. Another intriguing observation was that only in the presence of lithium coatings was there a

correlation between deuterium irradiation of the surface and the “behavior” change of the O(1s) and C(1s) peaks (Taylor et al. (2011)).

As already presented in the first two sections of this chapter the previous experience with molecular dynamics simulations of plasma-surface interactions (Krstic et al. (2007b); Dadras and Krstic (2011)) has shown that simulation and experiment in chemical sputtering of carbon upon bombardment by deuterium can reach a significant level of agreement if atomistic simulations mimic the experiment as close as possible. Since our current quantum-classical approach would be too costly to allow for simulation cells larger than a few hundred atoms, resulting in maximum penetration depths of about 1 nm, and therefore impact deuterium energies of about 5 eV, while the experimental data were obtained at hundreds eV (and ≥ 1 keV), a candidate for possible disagreement between theory and experiment is the difference in impact energies. Since most of the chemistry between impact D and the surface happens at the end of the impact D cascade, when the D is almost thermalized with the other atoms in the surface, it was logical to assume that impact energy will not have effects in the qualitative conclusions on the deuterium chemistry. The Purdue group has performed two independent experiments with XPS diagnostics, bombarding a lithiated ATJ graphite sample by deuterium at 200 eV and 50 eV (Taylor and Allain (2011)). As can be seen in figure 3.10, the experiment convincingly illustrates that the in-surface chemistry qualitatively does not depend on the D impact energy.

Another experiment of the Purdue group, inspired by our simulation findings in this section, shows that the positive features of the lithium coating are connected somehow to the larger than expected concentrations of oxygen in the surface. Thus, in non-lithiated graphite they find at most 5% of oxygen in the surface, which is increased to 10% with lithiation. But, bombardment with the low-energy deuterium elevates the content of oxygen in the near-interface surface to more than 20%, sometimes exceeding 40% in the zone of interface (figure 3.11).

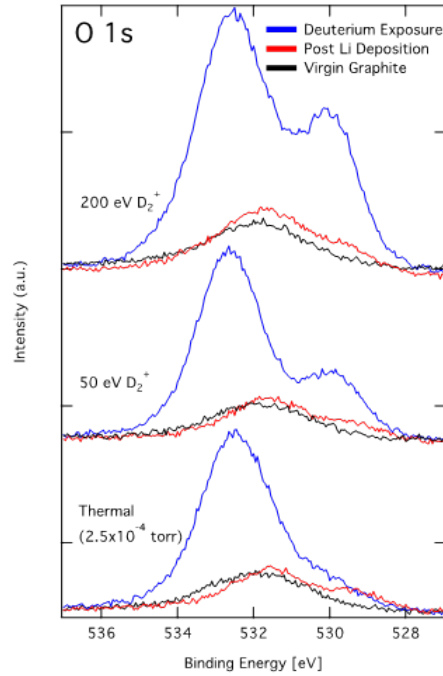


Figure 3.10: XPS measurement of oxygen diagnostics at 200 eV and 50 eV impact deuterium. The control group at thermal energies is also shown; figure from Taylor and Allain (2011).

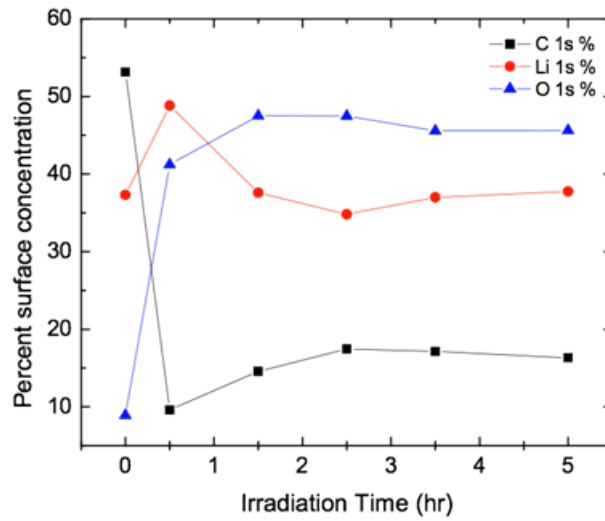


Figure 3.11: Cumulative surface concentration of O, Li and C upon deuterium bombardment

Our following calculations show that the results of simulation do agree with experiments qualitatively if the concentration of oxygen in the surface reaches or exceeds that of the lithium.

We use a simulation cell of a few hundred atoms, that was created by randomly seeding Li and/or O in amorphous hydrogenated carbon, replacing hydrogen by lithium and/or oxygen, followed by quantum-mechanical energy minimization and thermalization to 300 K. As expected, during the optimization, the simulation cell swelled about 30% to allow Li and O to create their extended bond lengths. The swelling decreased the effective carbon density. The cell was cut into a rectangular box with an approximate length of 1.5 nm, x-y periodic boundary conditions applied, and then optimization and thermalization of the periodic cell was repeated, resulting in slabs, that were periodic in x-y directions with a period of 14 Å while its thickness in the z-direction was close to 20 Å. The slabs were bombarded by 5 eV D atoms, perpendicularly to the free cell interface (in the z-direction)—see figure 3.1b. 5004 random trajectories were simulated for each surface, each evolving in a separate core of Cray XT5 of NICS (Kraken), with the time step of 1 fs. About 6 h was needed for most of the trajectories to finish their evolution, resulting either in reflection (fastest), retention and sputtering (slowest), thus requiring more than 120,000 CPU hours for all trajectories.

Once the sample cell is thermalized to 300 K, which defines the initial velocities of all atoms in the system except the impact D, the collision event evolves freely of any external scaling or thermostats. Normally, the lithium atoms are parameterized with s and p valence orbitals, and normally the s-orbitals are used in the dynamics. One can also use s *and* p-orbitals explicitly, to enable possible hybridization of the s and p lithium orbitals. We have done calculations with both s and s-p orbitals, leading to different numbers, but the qualitative conclusions of this work stay exactly the same in both approaches. Since s-p case leads to even stronger conclusions, we show here these results, while comparisons of the two groups of results we show in the Appendix. Finally, another parameter can be used for a case of poor numerical

convergence—the electronic temperature, which smears the molecular orbital energies across the homo-lumo gap. Here, 300 K was used for electronic temperature in all cases, except for the case of the Li-C system (with s-p basis), which required an electronic temperature of 1000K for smooth convergence.

Figure 3.12(a-d) shows the average distributions of charges of all atoms in the system which are not sputtered, for various cases of the target surfaces, and for impacting D; here, only cases when the D atom is retained are counted. The average charge of Li, C, and O is calculated for the final distribution of each retained trajectory, while the D charge is recorded at the last point of a retained trajectory. Therefore, for each trajectory any of Li, C, O, D appears once and so the heights of the peaks do not have any absolute meaning. The surfaces of a-C as well as a-C:Li/O with various contents of Li and O are considered. Figure 3.12(e-h) shows the integrated and normalized charge distributions of the figure 3.12(a-d). The impacting

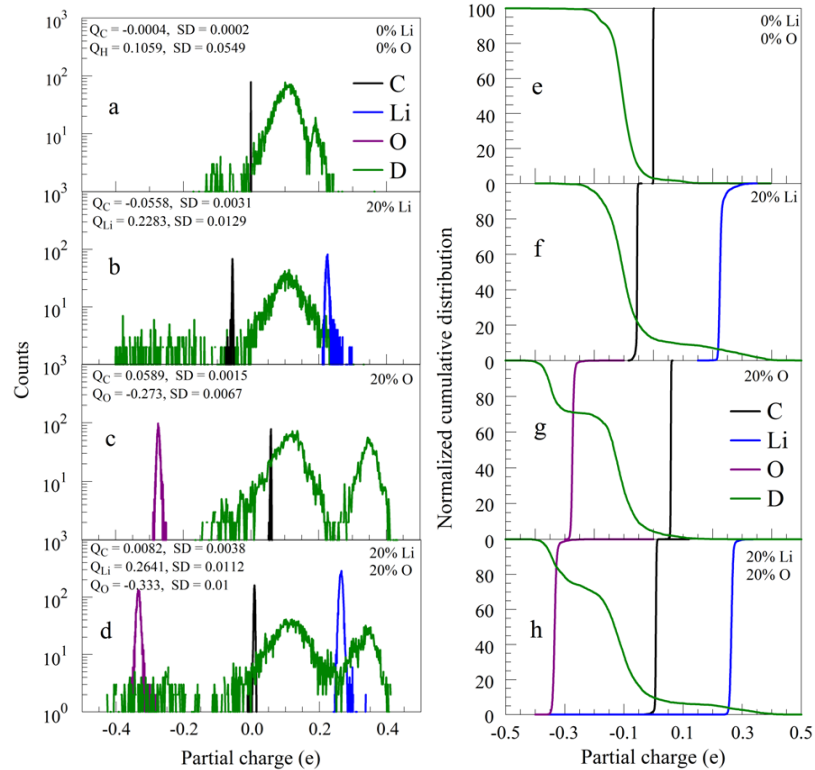


Figure 3.12: Distribution of charges in the systems (a - d) and normalized cumulative distributions of charges (e - h).

D is adapting to the charges of the target, in particular at its bonding site, so its partial charge indicates (in a statistical sense) to what atoms it is bonding, keeping the system quasi-neutral. For that reason the impact-D integral distribution of charges is shown multiplied with minus sign. As seen in figure 3.12f, less than 20% D atoms are in the vicinity of Li atoms or Li-C compounds. But, figure 3.12g, that contains only 20% O in carbon, shows that about 30% of D are in the vicinity of O and most of D is bound to the C-O compounds. This is confirmed in the case when there is an equal concentration (20%) of O and Li in the carbon. Apart from less than 10% of D that is bound in vicinity of Li, the rest is bound to O or C-O compounds, indicating that when there is a comparable quantity of oxygen to lithium, the chemistry of the retained D is dominantly guided by the presence oxygen.

The findings of figure 3.12 are fully confirmed in figure 3.13, which shows distributions of the nearest neighbors to retained D (a-d), as well as integral distributions (e-h).

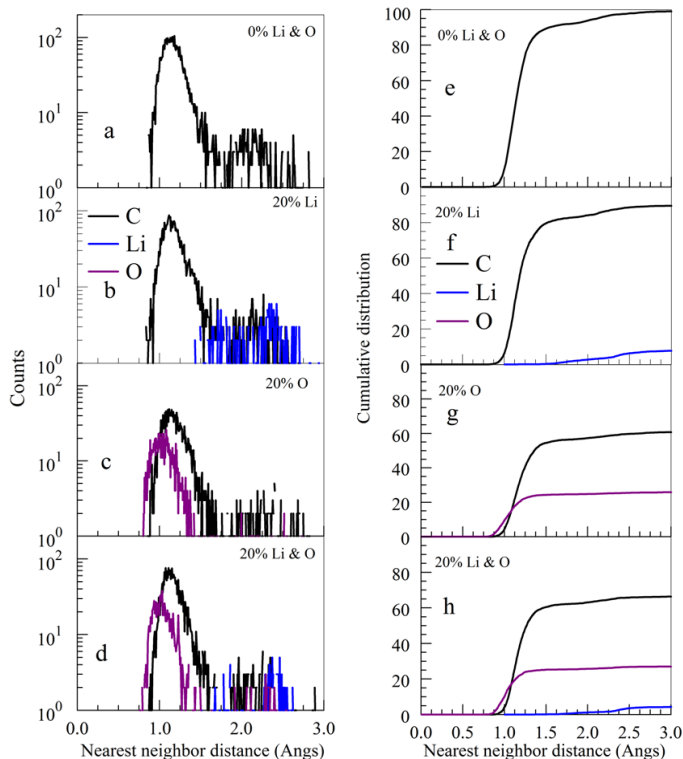


Figure 3.13: Distributions of nearest neighbors to retained D (a - d) and their cumulative distributions (e - h).

butions of the nearest neighbors (e-h). Even when there is an equal quantity of O and Li in the carbon, the oxygen by far dominates as the nearest bonding neighbor.

As a sanity check to insure that the simulations have nearly completed their evolution, figure 3.14 shows final kinetic energy distributions of the D retained in the surface. Results show that D is mostly in its classical “ground-state,” i.e. at the bottom of the well, close to zero eV. The energies are classical vibrational energies, and they have a continuous distribution, with half-widths less than 0.2 eV.

Realistic experimental conditions would be better approximated if one saturates the Li-C-O surface with deuterium (hydrogen) prior to each prescribed simulation. However, since the saturation process is causal, this would require much more computational effort if done with the SCC-DFTB method. Some combination of the CMD and the DFTB is a must for creation of a saturated (steady-state) surfaces (Krstic et al. (2007b)) and is a subject for future work. Nevertheless, to check the influence of the hydrogen accumulation (figures 3.15 and 3.16), we randomly seeded

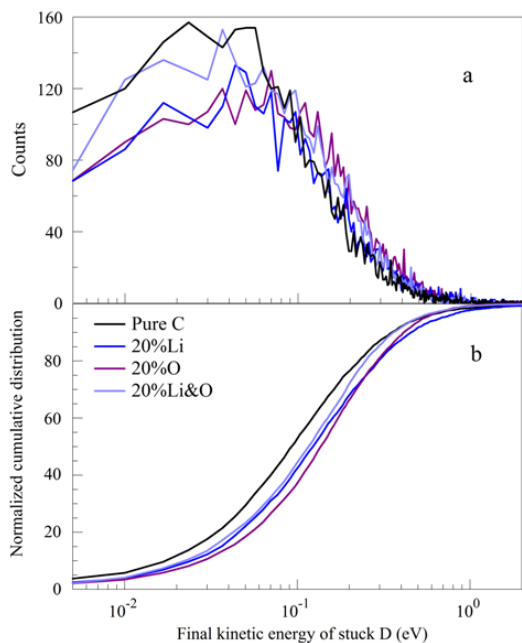


Figure 3.14: Distribution of the final kinetic energies of the retained D (a), and their normalized cumulative distributions (b).

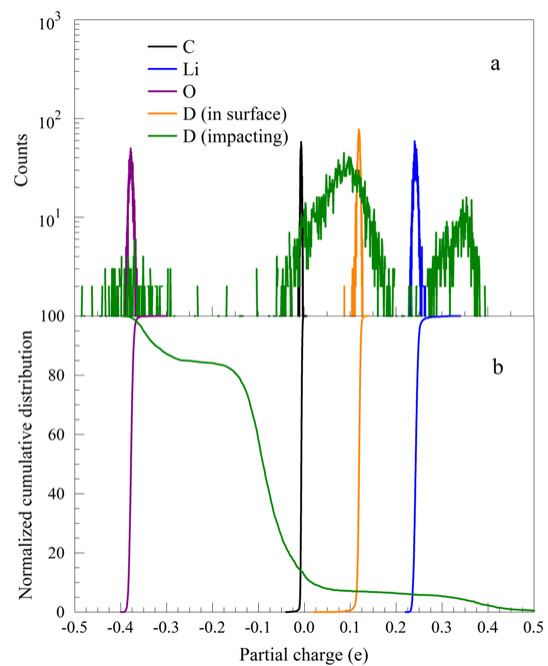


Figure 3.15: The partial charge distributions for a “cumulative” D case.

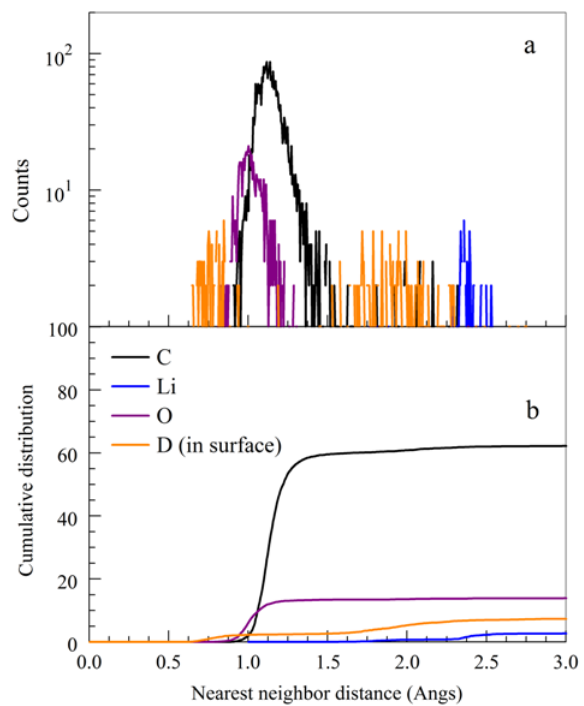


Figure 3.16: The nearest neighbor distributions for a “cumulative” D case.

a surface, such that Li, O and D have the same (16%) concentrations in carbon, the conclusion drawn from figures 3.12 and 3.13 are still valid, as can be seen in figures 3.15 and 3.16.*

Figure 3.17 presents the retention probabilities and sputtering yields of various surfaces upon impact of 5 eV D. The obtained sputtering yields, in particular for the 20% Li surface, are relatively large in comparison to those obtained by bombardment of D on deuterated carbon (Krstic et al. (2007b)). The bonding of Li to C is about 2 eV, i.e. more than two times smaller than C-C binding (4.5 eV), therefore the high sputtering yields (relative to carbon) for lithium are not surprising, and were seen in the experiments of Yagi et al. (2003) and Kato et al. (1999). However, the carbon sputtering is also high, which partially opposes experiments of Yagi et al. (2003); Kato et al. (1999) who found that intercalated lithium into graphite suppresses chemical and physical carbon sputtering of hydrogenated graphite surfaces.

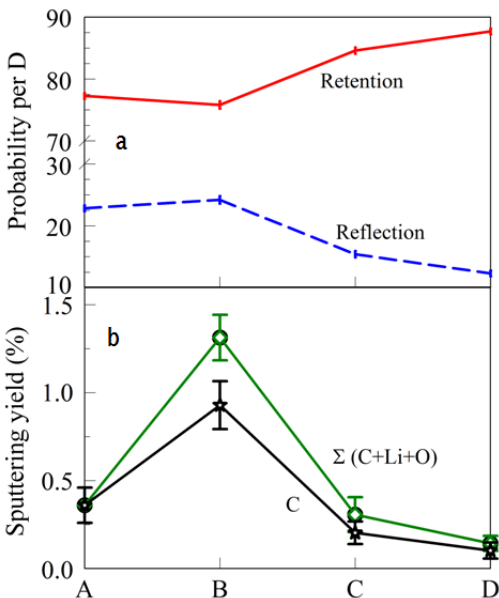


Figure 3.17: a) Retention and reflection probabilities of impact D, and b) total and C sputtering yields of the various cases. A: a-C; B: 20% Li; C: 20% Li and O; D: 20% O in C.

*We state here that this system also required an elevated electronic temperature of 600 K to converge.

The present findings indicate that suppression of the carbon sputtering by lithium's presence might not be caused by the Li chemistry. As one would expect from the results in figures 3.12-3.17, while Li does not do anything to suppress sputtering and enhance retention of D, the presence of oxygen with or without Li does this job. Cummulation of deuterium does not change this conclusion.

Our findings, consistent with XPS experimental data, have far reaching consequences: It is not lithium that suppresses erosion of carbon, and increases retention of deuterium. The oxygen plays the key role in the binding of hydrogen, while lithium is a catalyst of the process of oxygen accumulation in the surface, i.e. it is the oxygen getter. We find that if there is a significant amount of oxygen in the surface, comparable to the lithium content, oxygen becomes the main player. Lithium has a minor influence on the D chemistry in C. These conclusions are in harmony with many laboratory and reactor-based experiments of [Taylor and Allain \(2011\)](#); [Skinner et al. \(2011\)](#).

3.3.1 Isotopic Effects

The chemistry and sputtering/reflection dynamics in a 20% lithiated and 5% oxygenated carbon slab, bombarded by both slow deuterium (5 eV) and hydrogen (2.5 eV) atoms, was studied by [Krstic et al. \(2011\)](#).[†] Comparing the penetration depths of the impacting atoms into Li-C-O mixture with those previously found in hydrogenated carbon (figure 3.18) from [Krstic et al. \(2007b\)](#). In both cases of figures 3.18 and 3.19 the surfaces swell by bombardment; about 75% of impact deuterium and 67% of hydrogen in our simulations was retained (exact numbers for D and H are shown in figure 3.19).

For 5 eV impact energy in figure 3.18, the penetration of D in a-C:D is peaked at about 2 Å, following a distribution which has the half-width of about 5 Å. On the other hand the penetration of D into Li-C-O mixture is peaked around 5 Å. However,

[†]We have used only the s-basis for the following calculations.

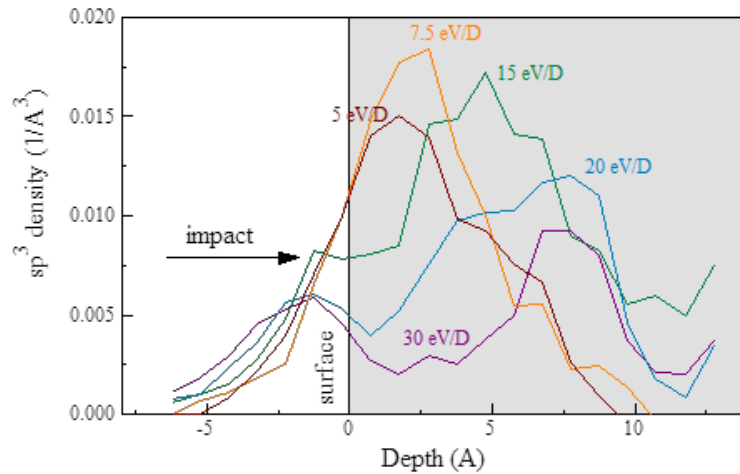


Figure 3.18: Penetration depth of deuterium into deuterated carbon of 2 g/cm³, for various impact energies of D. Figure from Krstic et al. (2007b).

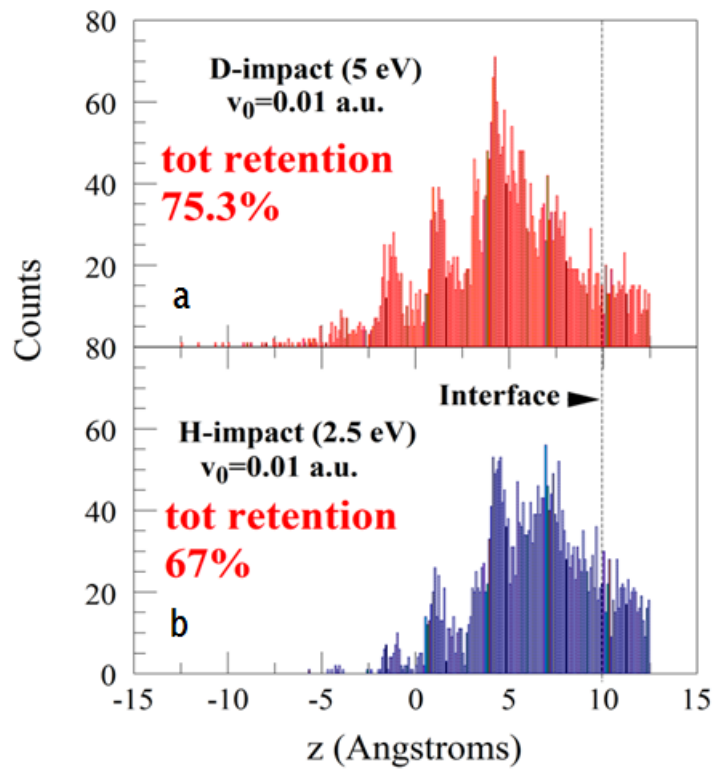


Figure 3.19: Penetration distributions of a) D and b) H into LiCO mixture. Interface of the surface with vacuum prior to bombardment is presented by vertical dashed line perpendicularly to the interface. Figure from Krstic et al. (2011).

its half-width is difficult to define, because the penetration distribution contained a series of narrow peaks arising from the nano-scale surface structure. The penetration of H shows a similar oscillatory structure, somewhat shifted toward shallower depth, showing a weak isotopic effect. A deeper penetration of D into Li-C-O than into a-C:D is a consequence of the reduced density of C in Li-C-O, as well as the saturated deuterization of the a-C:D in figure 3.18.

An interesting result of the present work arises from analysis of the distributions of the charges in figure 3.20; where it is observed that the charge distributions show almost no isotopic effects. However, as can be seen from figure 3.21, there is a significant isotope effect in the sputtering yields: the yields by D impact are about a factor three larger than those by H impact.

Most of this isotope effect can be explained by having in mind that the transfer of energy in an elastic binary collision of a projectile of kinetic energy E_1 and mass m_1 on a target atom of mass m_2 is

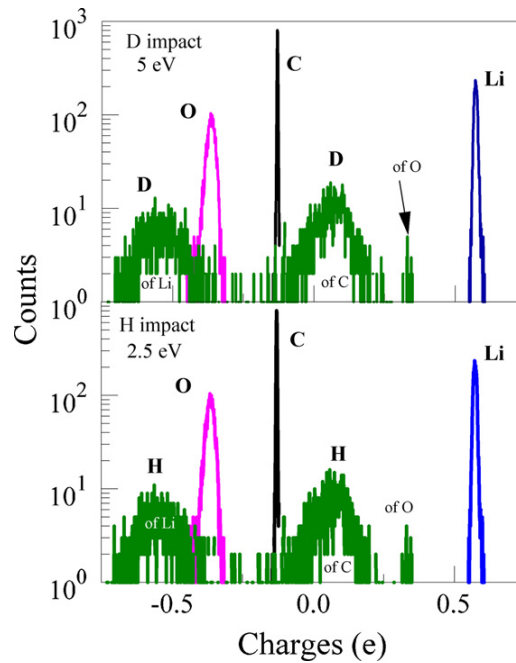


Figure 3.20: Charge distributions of a) D and b) H, as well as of Li, C and O upon the retention process. Figure from [Krstic et al. \(2011\)](#).

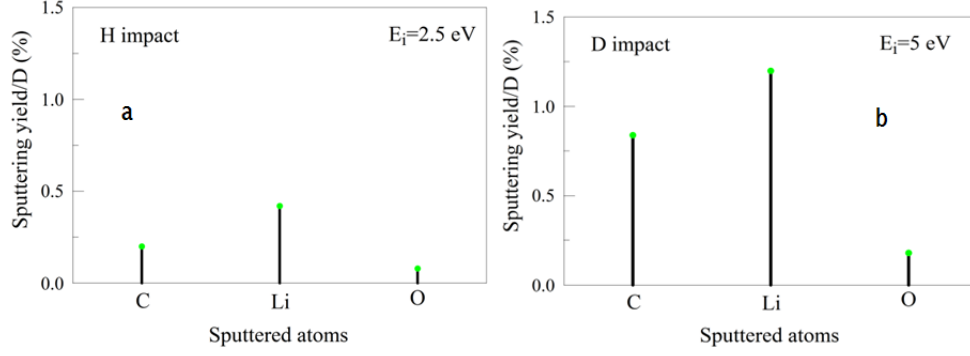


Figure 3.21: Sputtering yields (in %) of the LiCO surface by a) H impact and b) D impact. Figure from [Krstic et al. \(2011\)](#).

$$\Delta E = \frac{4m_1m_2E_1}{(m_1 + m_2)^2} \quad (3.1)$$

Considering the fact that the yields in figure 3.21 are defined per impact particle (rather than per nuclei), we obtain $\Delta E_D/\Delta E_H \approx 3.2$ for the energy transferred to Li, which is close to the found ratio of 3.

It is interesting to show the kinetic energy distribution of the reflected deuterium and hydrogen atoms (figure 3.22). Both distributions have a Maxwellian shape whose high energy wings are well fitted to the Boltzmann distribution corresponding to an energy of 0.5 eV for D, and 0.6 eV for H. This surprising thermalization can be realized if the impact particle makes a cascade through the surface before the ejection through the “hot” void created by the particle.

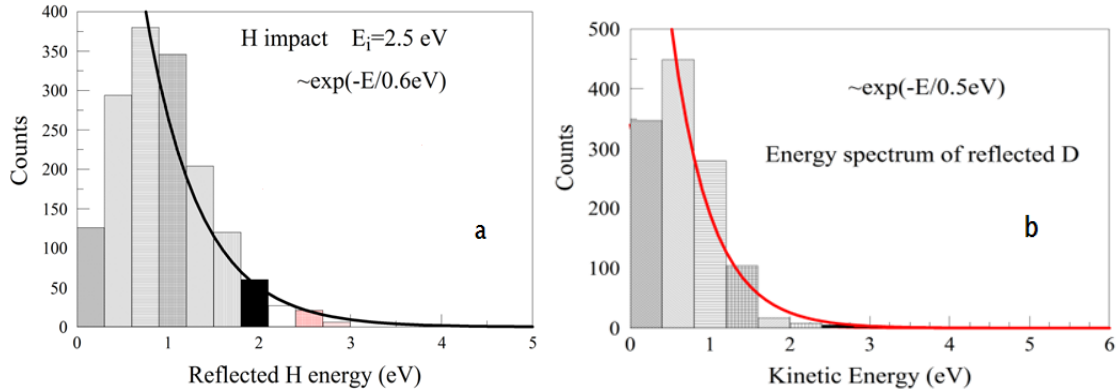


Figure 3.22: Energy distribution of the reflected (a) hydrogen, (b) deuterium atoms. Solid lines: Boltzmann distribution fit. Figure from [Krstic et al. \(2011\)](#).

3.3.2 Comparison with PW-DFT

From [Krstic et al. \(2011\)](#) a comparison of two static calculations was made between SCC-DFTB and Plane-Wave DFT (PW-DFT) ([Allouche and Ferro \(2006\)](#); [Allouche et al. \(2005\)](#)), for a double-layer graphite infinite sheet (x-y periodic boundary conditions applied to the graphite cell in figure 3.23), varying positions of Li and H with respect to the graphene. A single H is bonded to the graphene from the top and configuration optimized (configuration A); a Li atom is bonded to a C atom at the top, configuration optimized and then the hydrogen atom placed at different distances from the Li atom, above the top layer (configurations B-D); finally a lithium atom is intercalated between the graphite layers, and H bound above the top layer and optimized (configuration E).

A good comparison of the absolute values obtained by PW-DFT and SCC-DFTB is hard to obtain. However, as with comparisons of the values obtained by various functionals in DFT calculations, here we consider the qualitative trend in the curves. Figure 3.24 shows a comparison of the charges obtained by the two methods, for the described configurations of the Gr-Li-H. The charges of Li and H follow the same trend. While H shows even a good agreement of quantitative values of the charges, Li charges by SCC-DFT are almost factor two larger than with PW-DFT.

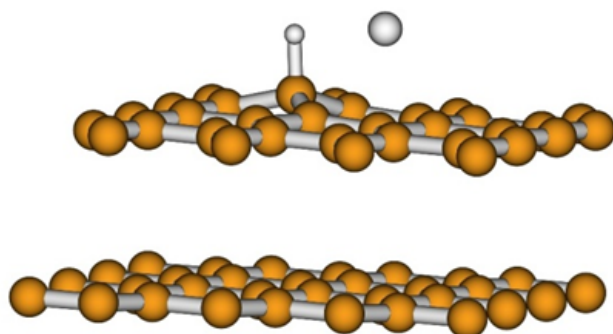


Figure 3.23: Double-layer graphitic slab with Li and H atoms. Figure from [Krstic et al. \(2011\)](#).

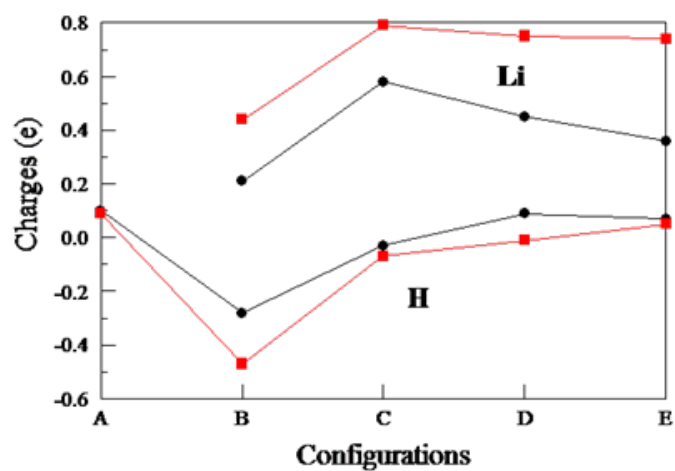


Figure 3.24: Charges of Li and H atoms for various positions of the H atom. AD: increasing distance LiH. E: corresponding to Li intercalated between two planes. Figure from [Krstic et al. \(2011\)](#).

Chapter 4

Conclusions

Fusion reactors, as commercial energy sources, have been a dream since the middle of the twentieth century; much progress has been made in determining reactor design to “ignite” a confined burning plasma. A key issue left to be resolved is the understanding and control of the plasma facing material components (e.g. the vessel wall, divertor, limiters, RF-antennas, etc.). Of particular importance, are minimizing erosion rates of materials in the divertor surfaces, which experience the highest flux of plasma particles, and suppressing retention of tritium in the walls. Atomistic molecular dynamics simulations can offer a window into the chemical/physical processes taking place at the Plasma Material Interface (PMI). We use a Monte Carlo technique to generate statistics on low energy deuterium impacting various amorphous carbon surfaces containing mixtures of other elements (D, Li, and O), bombarding the same surface by several thousand independent random trajectories of the impacting particle.

The chemical sputtering of a-C:D surfaces bombarded by deuterium atoms has been studied over a range of temperatures and impact particle energies. Classical Molecular Dynamics (CMD), with the well-developed Reactive Empirical Bond-Order (REBO) hydrocarbon potentials, cannot be used to accurately model processes of thermal diffusion, which evolve at longer time-scales. We developed an

approach to emulate these thermal processes by artificially overheating the system to accelerate these effects. Results of our simulations, and comparison with experiments, supporting the hypothesis that the main reason for the observed decrease in hydrocarbon sputtering in experiments with increasing surface temperature (above 700 K) is thermally induced loss of hydrogen from the top layers of the a-C:D surface. The accumulation of hydrogen in carbon is the precursor for efficient hydrocarbon sputtering. This work was published in [Dadras and Krstic \(2011\)](#)

We have improved the REBO potentials along two fronts: for higher energy collisions (i.e. short-distance atom-atom interactions), where we have included the universal repulsive ZBL potential; we have fit the REBO potentials to additional small molecules. The changes resulted in better agreement with experiments of chemical sputtering in deuterium impact on hydrogenated carbon; this work was published in [Kent et al. \(2011\)](#). Also, we have developed a Bond-Order Potential (BOP) for the Li-C-H system, including Coulomb interactions between partial charges calculated by the Electronegativity Equilibration Method (EEM); this potential has not yet been thoroughly tested. Because of the need to recalculate charges by EEM, use of this BOP in CMD has not shown clear advantages in computational time over the quantum-classical approach, using the SCC-DFTB method. We have chosen the latter as our approach for the description of the PMI containing lithium.

We have shown, using quantum-classical molecular dynamics based on SCC-DFTB (with Slater-Kostner parameter files developed by [Morokuma \(2010\)](#)) that the role of oxygen, cumulated in the surface, is dominant in reactions of deuterium at the PMI—we have shown that surface-oxygenation leads to a higher deuterium retention and lower sputtering. Thus, we have demonstrated that lithium’s primary role is simply as an oxygen getter, which leads to oxygen confinement in the surface, and to the aforementioned effects. Lithium also has some role in the deuterium chemistry, but this is by far less pronounced than that of oxygen. This work was published in [Krstic et al. \(2011\)](#); [Dadras et al. \(2012\)](#).

The author has helped develop (in collaboration with the groups of H. Witek and S. Irle) Slater-Kostner parameters, where we have constructed the atomic orbitals by solving the Dirac-Kohn-Sham (DKS) equations with a Wood-Saxon confining potential; we have used the ZBL potential to determine repulsive splines at very short distances (below the level of about 1 Å)—repulsive potentials were determined by taking the difference between DFTB band energies and DFT total energies for various reference systems and fitting to splines. Two families of mixed material parameterizations have been developed: 1) H-He-C-O-Li-Mo and 2) H-He-C-Be-W. For the first family molybdenum and helium are included in addition to parameters of [Morokuma \(2010\)](#); these will be used to model current and future components of the Liquid-Lithium Divertor (LLD) with Mo tiles at NSTX. For the second family; these will aid in modeling the PMI in reactors such as ITER and DEMO; a comparison with proposed experiments at ORNL, Purdue, and UCSD is planned for future simulations.

The simulations shown in section 3.3, as well as those suggested for future work, represent (to the author’s knowledge) the first attempt at using a quantum-classical approach for atomistic simulations of the fusion-plasma material interface.

Bibliography

Bibliography

- Abell, G. C. (1985). Empirical chemical pseudopotential theory of molecular and metallic bonding. *Phys. Rev. B*, 31:6184–6196. [8](#), [11](#)
- Adelman, S. A. and Doll, J. D. (1976). Generalized langevin equation approach for atom/solid-surface scattering: General formulation for classical scattering off harmonic solids. *The Journal of Chemical Physics*, 64(6):2375–2388. [8](#)
- Allouche, A. and Ferro, Y. (2006). First-principles study of electronic properties of hydrogenated graphite. *Phys. Rev. B*, 74:235426. [61](#)
- Allouche, A., Ferro, Y., Angot, T., Thomas, C., and Layet, J.-M. (2005). Hydrogen adsorption on graphite (0001) surface: A combined spectroscopy–density-functional-theory study. *The Journal of Chemical Physics*, 123(12):124701. [61](#)
- Andreani, R., Diegele, E., Gulden, W., Lahsser, R., Maisonnier, D., Murdoch, D., Pick, M., and Poitevin, Y. (2006). Overview of the european union fusion nuclear technologies development and essential elements on the way to demo. *Fusion Engineering and Design*, 81(1-7):25 – 32. Proceedings of the Seventh International Symposium on Fusion Nuclear Technology. [35](#)
- Balden, M. and Roth, J. (2000). New weight-loss measurements of the chemical erosion yields of carbon materials under hydrogen ion bombardment. *Journal of Nuclear Materials*, 280(1):39 – 44. [xi](#), [34](#), [35](#), [36](#), [37](#), [39](#), [40](#), [41](#), [42](#), [43](#), [45](#)

- Bell, M. G., Kugel, H. W., Kaita, R., Zakharov, L. E., Schneider, H., LeBlanc, B. P., Mansfield, D., Bell, R. E., Maingi, R., Ding, S., Kaye, S. M., Paul, S. F., Gerhardt, S. P., Canik, J. M., Hosea, J. C., Taylor, G., and the NSTX Research Team (2009). Plasma response to lithium-coated plasma-facing components in the national spherical torus experiment. *Plasma Physics and Controlled Fusion*, 51(12):124054. [46](#)
- Bloch, F. (1928). *The Quantum Mechanics of Electrons in Crystal Lattices*. PhD thesis, University of Leipzig. [22](#)
- Bremen (2010). Bremen Center for Computational Materials Science; DFTB parameters; <http://www.dftb.org/>. [32](#)
- Brenner, D. W. (1990). Empirical potential for hydrocarbons for use in simulating the chemical vapor deposition of diamond films. *Phys. Rev. B*, 42:9458–9471. [9](#), [12](#)
- Brenner, D. W., Shenderova, O. A., Harrison, J. A., Stuart, S. J., Ni, B., and Sinnott, S. B. (2002). A second-generation reactive empirical bond order (rebo) potential energy expression for hydrocarbons. *Journal of Physics: Condensed Matter*, 14(4):783. [9](#), [11](#), [12](#), [16](#), [36](#)
- Car, R. and Parrinello, M. (1985). Unified approach for molecular dynamics and density-functional theory. *Phys. Rev. Lett.*, 55:2471–2474. [21](#)
- Chadi, D. J. (1979). Atomic and electronic structures of reconstructed si(100) surfaces. *Phys. Rev. Lett.*, 43:43–47. [22](#)
- Dadras, J., Krstic, P., Taylor, C., Allain, J., Morokuma, K., Maeda, S., Jakowski, J., and Allouche, A. (2012). In preparation for Nature Communications. [46](#), [64](#)
- Dadras, J. and Krstic, P. S. (2011). Chemical sputtering of deuterated carbon surfaces at various surface temperatures. *Nuclear Instruments and Methods in Physics Research Section B: Beam Interactions with Materials and Atoms*, 269(11):1280

- 1283. INELASTIC ION-SURFACE COLLISIONS Proceedings of the 18th International Workshop on Inelastic Ion-Surface Collisions (IISC-18). [x](#), [xi](#), [34](#), [36](#), [37](#), [38](#), [41](#), [42](#), [43](#), [49](#), [64](#)
- Desclaux, J. (1970). Hartree fock slater self consistent field calculations. *Computer Physics Communications*, 1(3):216 – 222. [29](#), [32](#)
- Desclaux, J. (1975). A multiconfiguration relativistic dirac-fock program. *Computer Physics Communications*, 9(1):31 – 45. [29](#), [32](#)
- Doerner, R., Baldwin, M., Temmerman, G. D., Hanna, J., Nishijima, D., Roth, J., Schmid, K., Tynan, G., and Umstadter, K. (2009). Codeposition of deuterium with iter materials. *Nuclear Fusion*, 49(3):035002. [xi](#), [40](#), [41](#), [42](#), [43](#)
- Elstner, M., Porezag, D., Jungnickel, G., Elsner, J., Haugk, M., Frauenheim, T., Suhai, S., and Seifert, G. (1998). Self-consistent-charge density-functional tight-binding method for simulations of complex materials properties. *Phys. Rev. B*, 58:7260–7268. [22](#), [26](#), [27](#), [28](#), [48](#)
- Evtikhin, V. A., Lyublinski, I. E., Vertkov, A. V., Mirnov, S. V., Lazarev, V. B., Petrova, N. P., Sotnikov, S. M., Chernobai, A. P., Khripunov, B. I., Petrov, V. B., Prokhorov, D. Y., and Korzhavin, V. M. (2002). Lithium divertor concept and results of supporting experiments. *Plasma Physics and Controlled Fusion*, 44(6):955. [2](#)
- Fermi, E. (1927). Un metodo statistico per la determinazione di alcune priopriet dell’atomo. *Rend. Accad. Naz. Lincei.*, 6:602. [22](#)
- Feynman, R. P. (1939). Forces in molecules. *Phys. Rev.*, 56:340–343. [28](#)
- Froyen, S. and Harrison, W. A. (1979). Elementary prediction of linear combination of atomic orbitals matrix elements. *Phys. Rev. B*, 20:2420–2422. [22](#)

- Han, S. S., Van Duin, A. C. T., Goddard, W. A., and Lee, H. M. (2005). Optimization and application of lithium parameters for the reactive force field, reaxff. *The Journal of Physical Chemistry A*, 109(20):4575–4582. [17](#), [20](#)
- Hohenberg, P. and Kohn, W. (1964). Inhomogeneous electron gas. *Phys. Rev.*, 136:B864–B871. [22](#)
- Hoover, W. G. (1985). Canonical dynamics: Equilibrium phase-space distributions. *Phys. Rev. A*, 31:1695–1697. [8](#)
- Jacob, W. and Roth, J. (2007). *Sputtering by Particle Bombardment*, chapter Chemical Sputtering. Berlin. [36](#), [39](#), [40](#)
- Jakowski, J. (2011). personal communication. [48](#)
- Janak, J. F. (1978). Proof that $\frac{\partial e}{\partial n_i} = \epsilon$ in density-functional theory. *Phys. Rev. B*, 18:7165–7168. [26](#)
- Juslin, N., Erhart, P., Traskelin, P., Nord, J., Henriksson, K. O. E., Nordlund, K., Salonen, E., and Albe, K. (2005). Analytical interatomic potential for modeling nonequilibrium processes in the W-C-h system. *Journal Of Applied Physics*, 98(12):123520. [16](#)
- Kato, S., Watanabe, M., Toyoda, H., and Sugai, H. (1999). Laboratory experiment on lithium chemistry and its application to effective wall conditioning. *Journal of Nuclear Materials*, 266-269:406 – 411. [56](#)
- Kent, P., Dadras, J., and Krstic, P. (2011). Improved hydrocarbon potentials for sputtering studies. *Journal of Nuclear Materials*, 415(1, Supplement):S183 – S186. Proceedings of the 19th International Conference on Plasma-Surface Interactions in Controlled Fusion. [ix](#), [x](#), [xii](#), [12](#), [13](#), [14](#), [15](#), [45](#), [46](#), [64](#)
- Kohn, W. and Sham, L. J. (1965). Quantum density oscillations in an inhomogeneous electron gas. *Phys. Rev.*, 137:A1697–A1705. [22](#)

- Krstic, P., Reinhold, C., and Stuart, S. (2009). Plasma-surface interactions of hydrogenated carbon. *Nuclear Instruments and Methods in Physics Research Section B: Beam Interactions with Materials and Atoms*, 267(4):704 – 710. Proceedings of the 17th International Workshop on Inelastic Ion-Surface Collisions. [36](#), [38](#), [40](#)
- Krstic, P. S., Allain, J. P., Allouche, A., Jakowski, J., Dadras, J., Taylor, C. N., and Yang, Z. (2011). Dynamics of deuterium retention and sputtering of li-c-o surfaces. *Fusion Engineering and Design*. [xii](#), [xiii](#), [46](#), [57](#), [58](#), [59](#), [60](#), [61](#), [62](#), [64](#)
- Krstic, P. S., Reinhold, C. O., and Stuart, S. J. (2007a). Chemical sputtering by impact of excited molecules. *EPL (Europhysics Letters)*, 77(3):33002. [36](#), [38](#)
- Krstic, P. S., Reinhold, C. O., and Stuart, S. J. (2007b). Chemical sputtering from amorphous carbon under bombardment by deuterium atoms and molecules. *New Journal of Physics*, 9(7):209. [xii](#), [36](#), [38](#), [40](#), [45](#), [48](#), [49](#), [54](#), [56](#), [57](#), [58](#)
- Kugel, H. W. (2010). APS-DPP talk from http://nstx.pppl.gov/DragNDrop/Scientific_Conferences/APS/APS-DPP_06/Contributed%20posters/QP1.6-Kugel-Lithium.pdf. [x](#), [3](#)
- Marmar, E., Allen, S., Bell, M., Bonoli, P., Heidbrink, B., Knowlton, S., Najmabadi, F., Neilson, H., Peng, M., Snyder, P., Strait, T., Tynan, G., and Uckan, N. (2009). Report of the burning plasma organization on planning for us participation in iter. From http://burningplasma.org/ref/bpo_iter_research_20090903.pdf. [35](#)
- Mech, B., Haasz, A., and Davis, J. (1998). Isotopic effects in hydrocarbon formation due to low-energy h+/d+ impact on graphite. *Journal of Nuclear Materials*, 255(2-3):153 – 164. [xi](#), [34](#), [35](#), [37](#), [43](#)
- Meyer, F., Harris, P., Zhang, H., Jacob, W., Schwarz-Selinger, T., and von Toussaint, U. (2011). Erosion of a-c:d thin films by low energy d+, , and ion beam irradiation. *Journal of Nuclear Materials*, 415(1, Supplement):S125 – S128. Proceedings of the

- 19th International Conference on Plasma-Surface Interactions in Controlled Fusion. [xii](#), [36](#), [43](#), [45](#), [46](#)
- Morokuma, K. (2010). personal communication. [32](#), [48](#), [64](#), [65](#)
- Mortier, W. J., Ghosh, S. K., and Shankar, S. (1986). Electronegativity-equalization method for the calculation of atomic charges in molecules. *Journal of the American Chemical Society*, 108(15):4315–4320. [17](#), [19](#), [20](#)
- Mulliken, R. (1955). Electronic population analysis on lcao-mo molecular wave functions. i. *J. Chem. Phys.*, 23:1833–1840. Provided by the SAO/NASA Astrophysics Data System. [26](#)
- Njo, S. L., Fan, J. F., and Van De Graaf, B. (1998). Extending and simplifying the electronegativity equalization method. *J Mol Catal A*, 134(1-3):79–88. [19](#)
- Norajitra, P., Abdel-Khalik, S. I., Giancarli, L. M., Ihli, T., Janeschitz, G., Malang, S., Mazul, I. V., and Sardain, P. (2008). Divertor conceptual designs for a fusion power plant. *Fusion Engineering and Design*, 83(7-9):893 – 902. Proceedings of the Eight International Symposium of Fusion Nuclear Technology. [35](#)
- Oliveira, A. F., Seifert, G., Heine, T., and Duarte, H. A. (2009). Density-functional based tight-binding: an approximate dft method. *J. Braz. Chem. Soc.* [23](#), [26](#), [27](#), [28](#)
- Organization, I. (2010). Iter: the world’s largest tokamak. From the ITER Organization; <http://www.iter.org/mach>. [x](#), [4](#)
- Parr, R. G. and Weitao, Y. (1985). *Density-Functional Theory of Atoms and Molecules (International Series of Monographs on Chemistry)*. Pergamon. [22](#)
- Porezag, D., Frauenheim, T., Kohler, T., Seifert, G., and Kaschner, R. (1995). Construction of tight-binding-like potentials on the basis of density-functional theory: Application to carbon. *Phys. Rev. B*, 51:12947–12957. [22](#), [28](#)

- Reinhold, C., Krstic, P., and Stuart, S. (2009). Hydrogen reflection in low-energy collisions with amorphous carbon. *Nuclear Instruments and Methods in Physics Research Section B: Beam Interactions with Materials and Atoms*, 267(4):691 – 694. Proceedings of the 17th International Workshop on Inelastic Ion-Surface Collisions. [36](#), [38](#)
- Salonen, E., Nordlund, K., Keinonen, J., and Wu, C. H. (2001). Swift chemical sputtering of amorphous hydrogenated carbon. *Phys. Rev. B*, 63:195415. [x](#), [35](#), [36](#), [40](#), [42](#), [43](#)
- Seifert, G., Porezag, D., and Frauenheim, T. (1996). Calculations of molecules, clusters, and solids with a simplified lcao-dft-lda scheme. *International Journal of Quantum Chemistry*, 58(2):185–192. [22](#)
- Skinner, C., Allain, J., Blanchard, W., Kugel, H., Maingi, R., Roquemore, L., Soukhanovskii, V., and Taylor, C. (2011). Deuterium retention in nstx with lithium conditioning. *Journal of Nuclear Materials*, 415(1, Supplement):S773 – S776. Proceedings of the 19th International Conference on Plasma-Surface Interactions in Controlled Fusion. [57](#)
- Slater, J. C. and Koster, G. F. (1954). Simplified lcao method for the periodic potential problem. *Phys. Rev.*, 94:1498–1524. [22](#)
- Stuart, S. J., Krstic, P. S., Embry, T., and Reinhold, C. O. (2007). Methane production by deuterium impact at carbon surfaces. *Nuclear Instruments and Methods in Physics Research Section B: Beam Interactions with Materials and Atoms*, 255(1):202 – 207. Computer Simulation of Radiation Effects in Solids. [36](#), [38](#)
- Stuart, S. J., Tutein, A. B., and Harrison, J. A. (2000). A reactive potential for hydrocarbons with intermolecular interactions. *The Journal of Chemical Physics*, 112(14):6472–6486. [11](#), [12](#)

- Taylor, C., Allain, J., Heim, B., Krstic, P., Skinner, C., and Kugel, H. (2011). Surface chemistry and physics of deuterium retention in lithiated graphite. *Journal of Nuclear Materials*, 415(1, Supplement):S777 – S780. Proceedings of the 19th International Conference on Plasma-Surface Interactions in Controlled Fusion. [47](#), [49](#)
- Taylor, C. N. and Allain, J. P. (2011). personal communication. [xii](#), [49](#), [50](#), [57](#)
- Tersoff, J. (1988). New empirical approach for the structure and energy of covalent systems. *Phys. Rev. B*, 37:6991–7000. [8](#), [10](#), [11](#)
- Thomas, L. H. (1927). The calculation of atomic fields. *Proceedings of the Cambridge Philosophical Society*, 23:542. Provided by the SAO/NASA Astrophysics Data System. [22](#)
- van Duin, A. C. T., Dasgupta, S., Lorant, F., and Goddard, W. A. (2001). Reaxff: A reactive force field for hydrocarbons. *The Journal of Physical Chemistry A*, 105(41):9396–9409. [17](#)
- Warshel, A. and Levitt, M. (1976). Theoretical studies of enzymic reactions: Dielectric, electrostatic and steric stabilization of the carbonium ion in the reaction of lysozyme. *Journal of Molecular Biology*, 103(2):227 – 249. [20](#)
- Witek, H. A., Kahler, C., Frauenheim, T., Morokuma, K., and Elstner, M. (2007). Relativistic parametrization of the self-consistent-charge density-functional tight-binding method. 1. atomic wave functions and energies. *The Journal of Physical Chemistry A*, 111(26):5712–5719. PMID: 17567112. [29](#), [32](#)
- Wong, C. (2009). Innovative tokamak demo first wall and divertor material concepts. *Journal of Nuclear Materials*, 390-391:1026 – 1028. Proceedings of the 18th International Conference on Plasma-Surface Interactions in Controlled Fusion Device. [35](#)

- Woods, R. D. and Saxon, D. S. (1954). Diffuse surface optical model for nucleon-nuclei scattering. *Phys. Rev.*, 95:577–578. [29](#)
- Yagi, H., Toyoda, H., and Sugai, H. (2003). Dramatic reduction of chemical sputtering of graphite under intercalation of lithium. *Journal of Nuclear Materials*, 313-316:284 – 287. *Plasma-Surface Interactions in Controlled Fusion Devices* 15. [56](#)
- Yang, Z. (2010). personal communication. [19](#)
- Ziegler, J. F., Biersack, J., and Littmark, U. (1985). *The Stopping and Range of Ions in Matter*. Pergamon. [12](#)

Appendix

Appendix A

In the following, calculations that only used the s-basis for lithium (i.e. did not allow for s-p hybridization) were made for surfaces that always contained a mixture of C-Li-O; e.g. rather than a surface containing 0% concentration of Li(O) and 20% of O(Li), these surfaces contained 5% of Li(O) and 20% of O(Li); we call such a surface an oxygen(lithium) dominant surface. Comparisons are made between these results and those in section 3.3, in particular with figures 3.12 and 3.13.

Figure A.1 shows the partial charge distributions for the various surfaces. By comparing with figure 3.12 it is seen that rather than being centered near $0.25e$, lithium's partial charge is more than twice as big, consistently around $0.65e$. This effect, for the case of equal concentrations (20%) of both Li and O, causes the oxygen to become more electro-negative with a peak near $-0.5e$ rather than around $-0.33e$. While the net effect on the carbon is small, it is noted that Q_C is consistently about $0.05e$ more negative than before.

The effect on nearest neighbors is minor, as can be seen by comparing figure A.2 (no s-p mixing in Li) with figure 3.13 (that allows for s-p mixing). All peaks are within the expected sums of the covalent radii of the different elements.

Figure A.3 shows a comparison of the penetration depth profiles for all the C-Li-O surfaces. It can be argued that adding lithium (using just the s-basis) to an oxygenated carbon surface slightly lowers the peak of the penetration depth, by about 0.5\AA . While, for the lithium dominant surface, using just the s-basis slightly increases

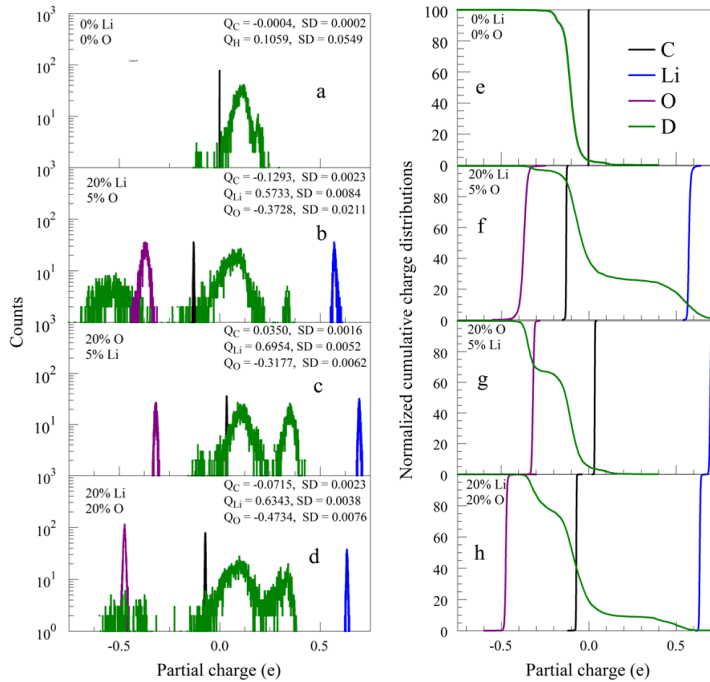


Figure A.1: Distribution of charges in the systems, when using only the s-basis in Li.

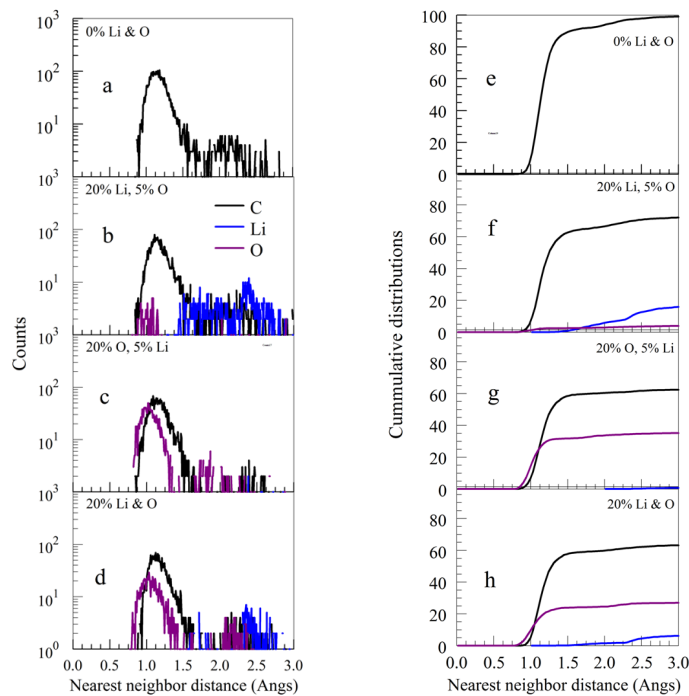


Figure A.2: Nearest neighbors distributions to impacting and stuck D, when using only the s-basis in Li.

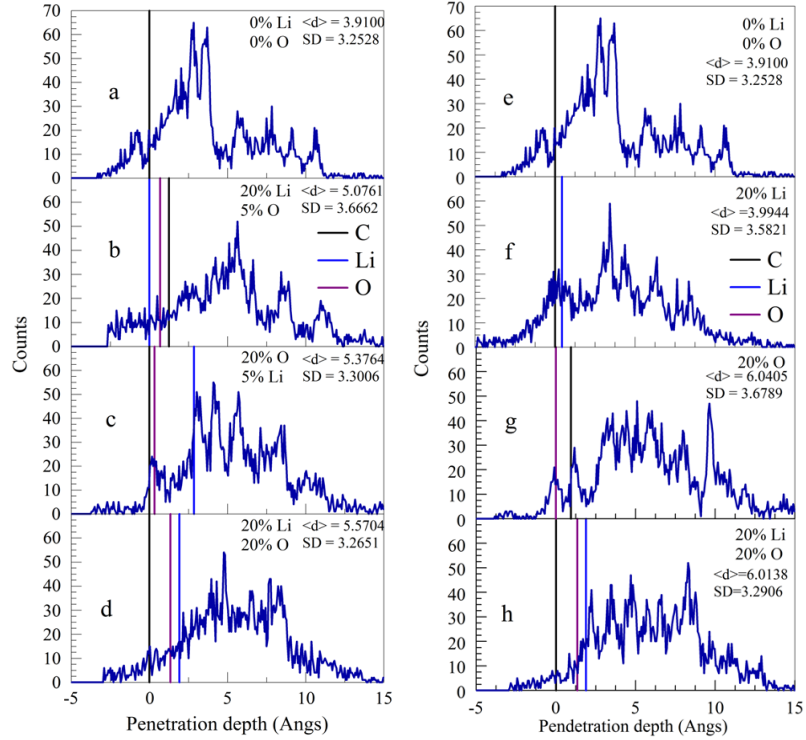


Figure A.3: Comparison of penetration depth profiles between (a - d) using only the s-basis in Li and (e - h) using the s-p basis.

the penetration depth (by approximately 1 Å). Also, the penetration depth is greater (by almost 2 Å) than the pure carbon surface. However, within the errors the means of all the penetration depths are the comparable.

The binding energy distributions of D to a surface are shown in figure A.4 for the various C-Li-O systems. Binding energies were calculated by taking the difference between the energies at the end of the MD run (when D is present), and then deleting the D atom and doing a single-point calculation. They are clearly dominated by D attaching to C. The lithium-dominant surface (without the s-p mixing) seems to allow for more D being bound to the surface by many-body and/or polar forces, rather than bonding to a particular atom, than the other cases.

Figure A.5 shows that by neglecting s-p hybridization, leads to only slight differences in the D-retention chemistry; though there is a notable decrease in C sputtering, there is also an increase in the Li sputtering. It is noted that the final

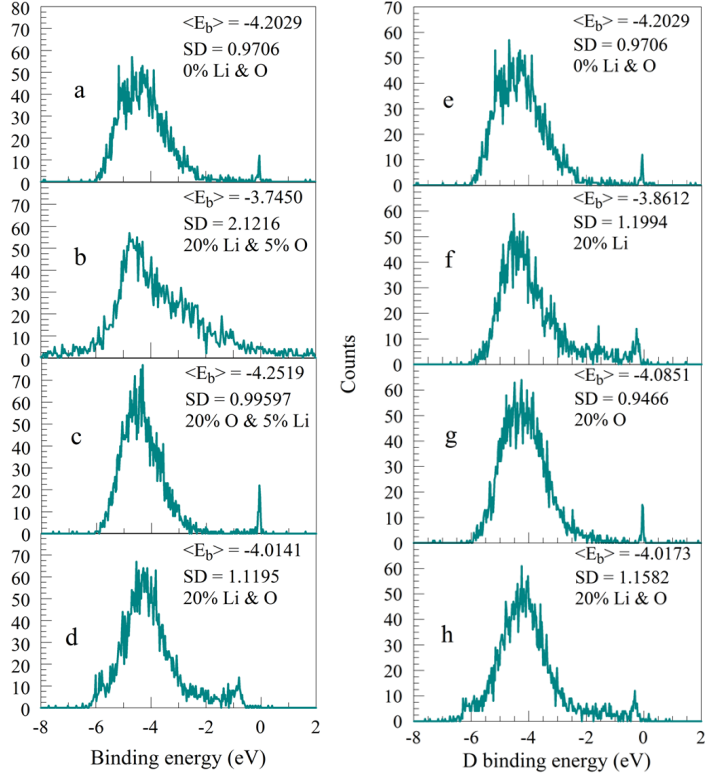


Figure A.4: Comparison of binding energy distributions between (a - d) using only the s-basis in Li and (e - h) using the s-p basis.

kinetic energy distributions of the retained D are peaked very near zero, with widths below 0.2 eV, regardless of the preferred basis.

For completeness, figure A.6 shows that the presence of D in the surface (i.e. the “cumulative” case) has very little affect either on the penetration depth profile or the surface binding energy.*

It was demonstrated that the exclusion of the virtual p-state in lithium has only minor effects on the qualitative picture of the chemistry of amorphous surfaces of C-Li-O bombarded by 5 eV D atoms. The most notable difference between the two cases is in the average partial charges of lithium; but, this has a minimal influence on the overall behavior of the system.

*Note that for the “cumulative” case the s-p basis in lithium is used.

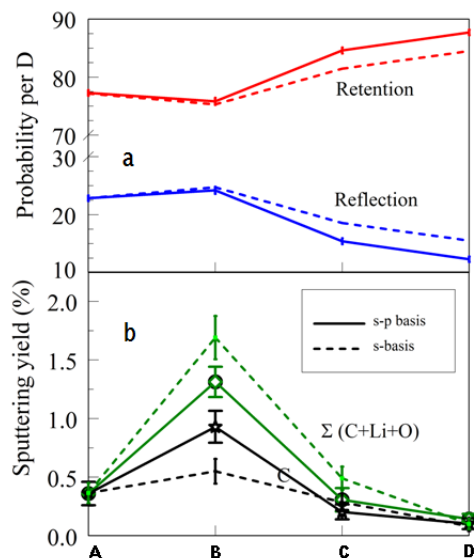


Figure A.5: Comparison of retention and reflection probabilities of impact D a), and total and C sputtering yields of the various cases A: a-C; B: 20% Li; C: 20% Li and O; D: 20% O in carbon b); using the s and s-p bases.

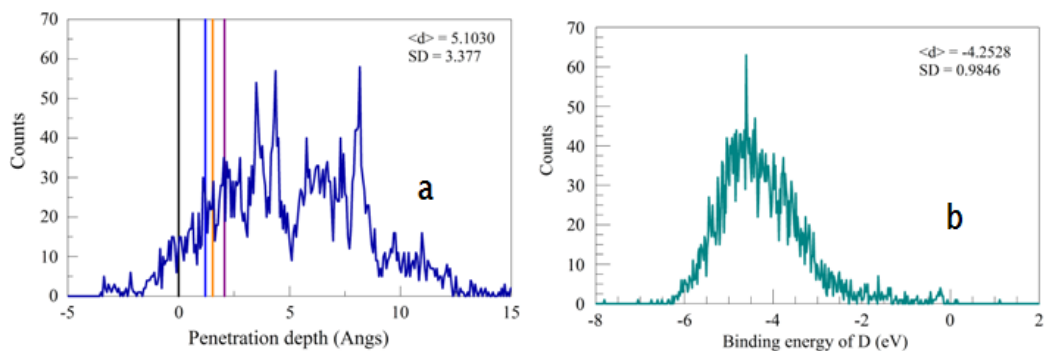


Figure A.6: a) penetration depth and b) binding energy for the “cumulative” surface, using the s-p basis in Li.

M. Jon Dadras was born and raised in Colorado. He received his B.A. in Physics and Mathematics from CU-Boulder in 2004. As an undergrad he did research in experimental condensed matter physics (looking at dielectric response in thin films of dipolar molecular rotors) and theoretical gravity/astrophysics (solving the Einstein equations for a sinusoidal potential and studying the cosmological effects). He completed his M.S. in experimental nuclear/particle physics with a thesis entitled “Polarimetry Studies for the NPDGamma Experiment at the SNS.” He finds theoretical atomic/molecular/chemical physics to be the happiest medium.